

Mesoscale Gravity Waves in Moist Baroclinic Jet–Front Systems

JUNHONG WEI AND FUQING ZHANG

Department of Meteorology, The Pennsylvania State University, University Park, Pennsylvania

(Manuscript received 12 June 2013, in final form 14 October 2013)

ABSTRACT

A series of cloud-permitting simulations with the Weather Research and Forecast model (WRF) are performed to study the characteristics and source mechanisms of mesoscale gravity waves in moist baroclinic jet–front systems with varying degrees of convective instability. These idealized experiments are initialized with the same baroclinic jet but with different initial moisture content, which produce different life cycles of moist baroclinic waves, to investigate the relative roles of moist processes and baroclinicity in the generation and propagation of mesoscale gravity waves. The dry experiment with no moisture or convection simulates gravity waves that are consistent with past modeling studies. An experiment with a small amount of moisture produces similar baroclinic life cycles to the dry experiment but with the introduction of weak convective instability. Subsequent initiation of convection, although weak, may considerably amplify the gravity waves that are propagating away from the upper-level jet exit region crossing the ridge to the jet entrance region. The weak convection also generates a new wave mode of shorter-scale wave packets that are believed to interact with, strengthen, and modify the dry gravity wave modes. Further increase of the moisture content (up to 5 times) leads to strong convective instability and vigorous moist convection. Besides a faster-growing moist baroclinic wave, the convectively generated gravity waves emerge much earlier, are more prevalent, and are larger in amplitude; they are fully coupled with, and hardly separable from, the dry gravity wave modes under the complex background moist baroclinic waves.

1. Introduction

As a ubiquitous buoyancy oscillation phenomenon in meteorology, gravity waves play an important role in a wide variety of atmospheric processes. Gravity waves can initiate and organize convection (Zhang et al. 2001), and generate and modulate atmospheric turbulence (Shapiro 1980). Furthermore, significant amounts of momentum and energy can be propagated and transferred by gravity waves (Eliassen and Palm 1961), which results in an impact on general circulation, especially for exchanges between the troposphere and stratosphere (Holton et al. 1995). Generally speaking, gravity waves can be generated and activated by topographic forcing, density impulses, convection, shear instability, and geostrophic adjustment related to jets, fronts, and/or sources of strong diabatic heating (Hooke 1986; Fritts and Alexander 2003; Kim et al. 2003). A better knowledge of

these processes demands a complete understanding of the mechanisms by which the gravity waves are generated, together with their characteristics, distribution, and variability.

Mesoscale gravity waves with horizontal wavelengths of 50–500 km are found to be prevalent in the vicinity of unbalanced upper-level jet streaks. Typically speaking, these jet–front gravity waves have vertical wavelengths of 1–4 km, periods of 0.5–4 h, amplitudes of 0.5–15 hPa (pressure perturbations at the surface), and phase velocities of 15–35 m s^{-1} (Uccellini and Koch 1987, hereafter UK87; Plougonven and Zhang 2014). Based on 13 observed gravity wave cases in the troposphere, UK87 suggested that the synoptic-scale baroclinic environment favorable for the generation of mesoscale jet–front gravity waves was the region bounded by the jet axis to the west or northwest, a surface front to the southeast, an inflection axis to the southwest, and a 300-hPa ridge axis to the northeast. This paradigm has been identified repeatedly in both observational studies (UK87; Schneider 1990; Fritts and Nastrom 1992; Ramamurthy et al. 1993; Bosart et al. 1998; Koppel et al. 2000; Rauber et al. 2001; Plougonven et al. 2003) and numerical investigations of the observed

Corresponding author address: Prof. Fuqing Zhang, Dept. of Meteorology, The Pennsylvania State University, University Park, PA 16802.
E-mail: fzhang@psu.edu

cases (Powers and Reed 1993; Pokrandt et al. 1996; Kaplan et al. 1997; Zhang and Koch 2000; Zhang et al. 2001; Koch et al. 2001; Zhang et al. 2003; Wu and Zhang 2004; Lane et al. 2004; Koch et al. 2005; Zhang et al. 2013).

Compared with the observations, numerical models are more advantageous to obtain the structures of mesoscale jet–front gravity waves. In particular, idealized simulations are helpful in the investigation of the gravity wave mechanism. One of the first attempts to simulate gravity waves initiated from idealized baroclinic waves was probably made by O’Sullivan and Dunkerton (1995, hereafter OD95). They used a 3D hydrostatic primitive equation model and demonstrated that gravity waves are generated in the exit region of the upper-tropospheric jet streaks, as the jet stream was distorted. Due to the coarse horizontal resolution (50–100 km) in OD95, the gravity waves have subsynoptic-scale characteristics with horizontal wavelengths of 600–1000 km, while mesoscale gravity waves are not found in their simulation. Zhang (2004, hereafter Z04) employed a 3.3-km high-resolution numerical simulation to reproduce gravity waves with a horizontal wavelength of about 100–200 km during the life cycles of baroclinic waves. It is shown that gravity waves in Z04 are generated in the exit region of upper-tropospheric jet streaks, and the spontaneous emissions of mesoscale gravity waves result from the continuous generation of imbalance, indicated by a nonlinear balance equation residual (Zhang et al. 2000, 2001). The horizontal wavelength of the jet–front gravity wave in Z04 is about 150 km, while the vertical wavelength is about 2.5 km, has a phase speed of 8 m s^{-1} , and its frequency is 4 times the Coriolis parameter, consistent with the linear gravity wave dispersion relation (Gill 1982). Wang and Zhang (2007) studied the sensitivity of mesoscale gravity waves to the baroclinicity of jet–front systems and concluded that the higher growth rate of baroclinicity could generate an increasing flow imbalance, which impacts the intrinsic frequency of gravity waves. Lin and Zhang (2008, hereafter LZ08) further studied the source of gravity waves in idealized baroclinic jet–front systems, using the same simulation as in Z04, and addressed the propagating characteristics and possible source mechanisms of jet-related gravity waves through 2D Fourier decomposition and ray-tracing techniques. Plougonven and Snyder (2007) further discussed the generation of inertia–gravity waves in idealized life cycles of baroclinic instability. Two substantially different life cycles of baroclinic instability are investigated: one is dominated by cyclonic behavior, and the other is dominated by anticyclonic behavior.

However, all of the aforementioned idealized baroclinic wave experiments were primarily focused on a

dry atmospheric process, which did not take moisture and heating into consideration. Although gravity waves have been discussed in recent studies using moist idealized baroclinic wave simulations, their research focus is either on mesoscale predictability (Tan et al. 2004; Zhang et al. 2007) or the mesoscale energy spectra (Waite and Snyder 2013) instead of the gravity waves. For either real-time observations (Koch and Dorian 1988; Bosart et al. 1998) or numerical simulations (Zhang and Fritsch 1988; Powers 1997; Zhang et al. 2001; Lane and Reeder 2001; Jewett et al. 2003), moist convection is closely linked with mesoscale gravity waves in the jet–front baroclinic wave. With the development of technology in computing capability, the use of convection-resolving mesoscale simulations with full moist physics to simulate gravity waves associated with moist baroclinic jet–front systems becomes possible. The role of moisture and heating in baroclinic jet–front systems is not yet clear. Moreover, gravity waves and moist convection are strongly coupled. On one hand, the vertical motion associated with gravity waves can organize and initiate moist convection (Powers 1997; Zhang et al. 2001). On the other hand, moist convection can generate gravity waves that propagate up into the middle atmosphere (Fritts and Alexander 2003). Also, moist convection is an active and significant contributor to the development of the baroclinic waves and flow imbalance. Recently, many studies have examined the gravity waves generated by moist convection (Lane and Reeder 2001; Lane and Zhang 2011), which focused on a homogeneous and tropical environment. However, there is still a lack of knowledge about the coupling and interactions of gravity waves with small-scale moist convection in complex large-scale baroclinic jet–front systems. The role of moisture in baroclinic jet–front systems is and will remain an active area of gravity wave research.

The aim of this paper, which is complementary to the work of Z04, is to explore the initiation and characteristics of mesoscale gravity waves in moist baroclinic jet–front systems using high-resolution idealized simulations. The experimental design will be presented in section 2, followed in section 3 by a description of the evolution and structure of idealized moist baroclinic wave simulations. Section 4 will present an analysis of the characteristics of the simulated gravity waves in the experiments. The evolution of simulated mesoscale gravity waves is explored in section 5. Sensitivity experiments about the effect of diabatic heating and horizontal resolution are presented in section 6. Section 7 presents a discussion on gravity wave variations under different convective instabilities. Section 8 contains a summary.

TABLE 1. Summary of the gravity wave characteristics in the numerical simulations. Column 1–8 represent the names of the wave packets (WPs), their observed horizontal wavelengths λ_h , observed vertical wavelengths λ_z , intrinsic frequencies Ω derived from dispersion relation, intrinsic horizontal phase speeds c_i derived from the dispersion relationship, calculated horizontal mean wind speeds U_h along wave vectors, observed ground-based phase speeds C_d , and calculated mean-flow-relative phase speeds C_{io} of gravity waves. Note that C_{io} and c_i generally agree quite well.

Wave packet-expt	λ_h (km)	λ_z (km)	Ω (10^{-4} s^{-1})	c_i (m s^{-1})	U_h (m s^{-1})	C_d (m s^{-1})	C_{io} (m s^{-1})
WP1-EXP00	90	1.7	3.9	-5.5	9.7	4.6	-5.1
WP1-EXP20	83	1.7	4.2	-5.5	9.8	4.7	-5.2
WP2-EXP00	310	2.8	2.2	-10.7	17.4	6.9	-10.4
WP2-EXP20	310	2.8	2.2	-10.6	17.7	6.9	-10.7
WP3-EXP00	80	6.2	14.6	-18.6	24.7	5.7	-19.0
WP3a-EXP20	68	4.9	13.5	-14.6	13.8	-0.8	-14.6
WP3b-EXP20	108	6.1	11.0	-19.0	26.4	7.9	-18.5
WP4-EXP00	96	2.0	2.5	-3.9	-2.7	-6.8	-4.1
WP4-EXP20	94	2.0	2.6	-3.9	-2.8	-7.1	-4.3
WP5s-EXP00	490	1.4	1.2	-9.4	18.0	8.3	-9.7
WP5n-EXP00	90	1.6	3.9	-5.5	13.4	7.6	-5.8
WP5s-EXP20	450	1.7	1.3	-9.6	18.3	9.0	-9.3
WP5n-EXP20	68	1.1	3.6	-3.9	13.9	10.4	-3.5
WP5nL-EXP20	193	2.4	2.9	-9.0	16.7	7.6	-9.0
WP5nH-EXP20	123	1.8	3.3	-6.5	16.0	9.7	-6.3
WP6-EXP20	62	2.8	9.2	-9.1	11.9	2.4	-9.5
WP6-EXP100	50	2.9	12.0	-9.5	15.8	6.3	-9.6

2. Experimental design

a. Model configuration

Instead of using the fifth-generation Pennsylvania State University–National Center for Atmospheric Research Mesoscale Model (MM5; Dudhia 1993) as in Z04, the current study employs the Advanced Research version of the Weather Research and Forecast model (ARW; Skamarock et al. 2008), version 3.4, for all of the simulations. The numerical experiments are performed on an f -plane domain with 10-km horizontal grid spacing, and 70 vertical layers with about 250-m vertical spacing at the surface coarsening to about 300-m vertical spacing at 12 km, and about 550-m vertical spacing at the upper boundary. The domain is configured in a rectangular channel: 4000 km in the zonal (x) direction, 8020 km in the meridional (y) direction, and 22 km in the vertical (z) direction. The channel has periodic boundary conditions in direction x and rigid boundaries (symmetric boundary conditions) in direction y . To prevent artificial wave reflection from the model top, Rayleigh damping is applied to the vertical velocity in the upper 5 km of the model domain (Klemp et al. 2008). Moist processes are parameterized with the Lin et al. (1983) microphysics scheme and no convection scheme is employed. Radiation, surface fluxes, and friction are all neglected. Except for the estimation of wave characteristics (e.g., Table 1), all the calculations are based on coarsened 500-m constant vertical grids from $z = 0.5$ to 2.0 km [e.g., Eq. (1) in section 3; cross-sectional

view]. The 3D simulated data demonstrated and calculated in this research mainly focus on the space from $y = 2000$ to 6000 km.

b. Initial conditions

The initial conditions consist of an idealized baroclinic jet and relative humidity field (Fig. 1a). The procedure for creating the initial balanced jet is similar to that used by Z04 and Wang and Zhang (2007). The initial moisture field follows Tan et al. (2004) and Zhang et al. (2007).

The initial idealized baroclinic jet is taken as the superposition of a simplified two-dimensional (2D) balanced zonal jet similar to Simmons and Hoskins (1978) and its most unstable normal mode with a 4000-km zonal wavelength. The balanced zonal jet is first calculated with a simplified 2D potential vorticity (PV) inversion (Davis and Emanuel 1991) in the y - z plane, and then expanded to three dimensions assuming zonal homogeneity. The geometry of the tropopause is specified as the thick line in the meridional cross section in Fig. 1a, with constant PV in both the troposphere (0.5 PVU) and stratosphere (4.0 PVU). Different from Z04, no mean zonal wind is subtracted from the balanced initial conditions, so that the baroclinic jet–front systems can propagate eastward throughout the periodic channel at the speed of about 14 m s^{-1} .

With the same initial idealized baroclinic jet, experiments with zero and full initial moisture content are performed. These experiments are called EXP00 and

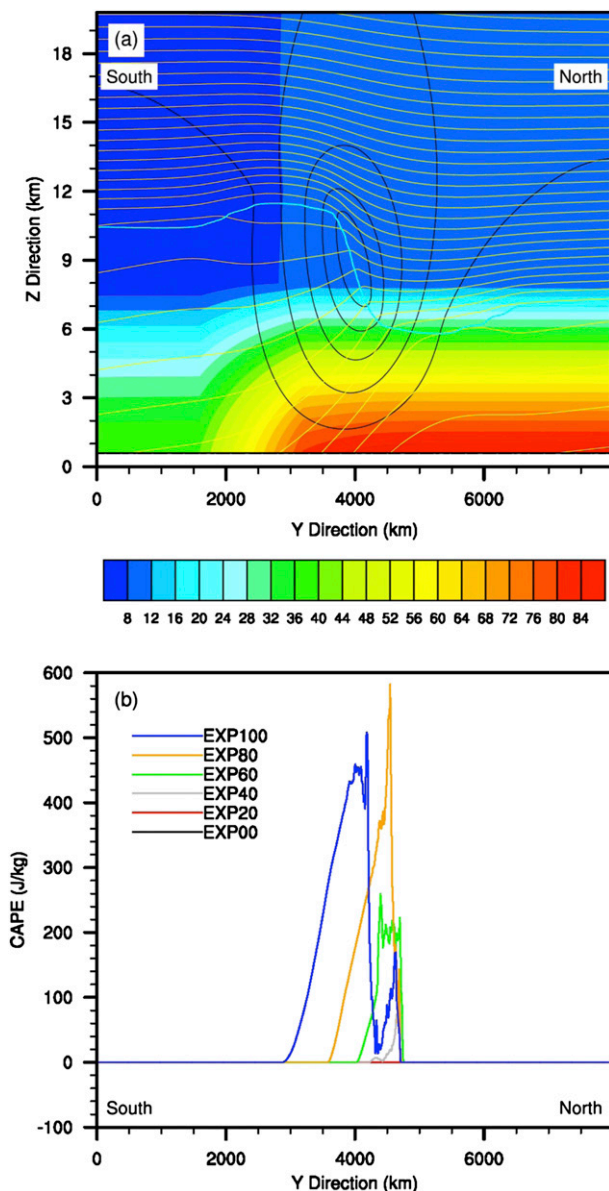


FIG. 1. (a) Vertical cross section of initial basic-state jet in EXP100. The black lines denote the horizontal velocity ($\Delta = 10 \text{ m s}^{-1}$), the yellow lines denote the potential temperature ($\Delta = 8 \text{ K}$), the blue thick lines denote the location of the tropopause where potential vorticity equals 1.5 PVU , and the shaded color denotes the relative humidity ($\Delta = 4\%$). (b) Meridional variation of zonal maximum CAPE (J kg^{-1}) for EXP00–EXP100 when the EKE-BW of each experiment reaches an amplitude of about $52.5 \text{ m}^2 \text{ s}^{-2}$.

EXP100, respectively. The initial moisture in EXP100 (shaded color in Fig. 1a) refers to the corrigendum for Tan et al. (2004). Unlike Fig. 1c in Tan et al. (2004), EXP100 manifests no initial maximum convective available potential energy (CAPE) due to the difference in thermodynamic variables (not shown). Several additional experiments (EXP80, EXP60, EXP40, and EXP20) are

also performed that reduce the initial relative humidity to a percentage (80%, 60%, 40%, and 20%, respectively) of the reference relative humidity profile used in EXP100 (Fig. 1a).

c. Sensitivity experiments

To test the sensitivity of mesoscale gravity waves to moist processes such as latent heating, fake dry (FD) and dry (DRY) experiments are employed. For example, EXP20-DRY represents DRY experiments with initial conditions as in EXP20. In FD, the microphysics scheme is turned on while the latent heating is set to zero. In DRY, the microphysics scheme is turned off. In addition, fake dry restart (FDR) and dry restart (DR) experiments are also performed. For example, EXP20-H100-FDR represents a 100-h moist simulation of EXP20 followed by FDR. To examine the sensitivity to model resolution, simulations EXP20–5KM, EXP40–5KM, EXP60–5KM, EXP80–5KM, and EXP100–5KM are performed exactly the same as in EXP20–EXP100 but with horizontal grid spacing of 5 km.

3. Simulated life cycles of dry and moist baroclinic waves

Figure 2a shows the time evolution of the mass-weighted average eddy kinetic energy (EKE) integrated over the entire 3D model domain from different moist wave life cycles with different initial moisture content. The mathematical definition of EKE is written as [e.g., Eq. (1) in Waite and Snyder (2013)]

$$\text{EKE} = \frac{\int \int \int \frac{1}{2} \rho (u'^2 + v'^2 + w'^2) dV}{\int \int \int \rho dV}, \quad (1)$$

where u' , v' , and w' are the perturbation components of zonal, meridional, and vertical winds, respectively. For the baroclinic wave component of EKE (EKE-BW; Fig. 2a), a low-pass filter (e.g., Wang and Zhang 2007; LZ08) is applied to extract wind perturbations with wavelengths over 600 km.

As indicated in Fig. 2a, the EKE-BW among all experiments remains indistinguishable during roughly the first 60 h. Compared to other experiments, the growth rate of baroclinic waves in EXP100 is considerably enhanced at around 85 h when EKE-BW first exceeds EXP80 by $1.0 \text{ m}^2 \text{ s}^{-2}$. To exemplify the difference in the growth rate among different experiments, this arbitrary threshold difference is not reached for EXP80 and EXP60 until 95 h, for EXP60 and EXP40 until 102 h, for EXP40 and EXP20 until 109 h, and for EXP20 and EXP00 until 111 h.

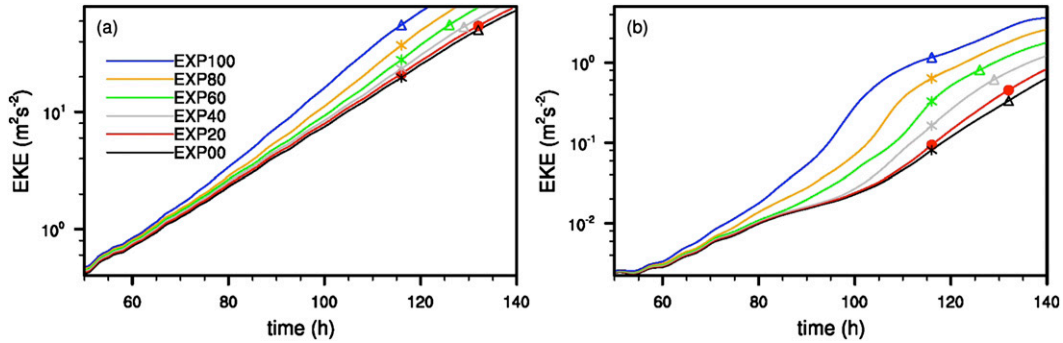


FIG. 2. Time series of EKE for (a) EKE-BW and (b) EKE-GW during 50–140 h. The *x* direction represents time (h) and the *y* direction represents EKE (m² s⁻²). The solid circles, open triangles, and asterisks denote the hours shown in Figs. 3, 4, and 5, respectively.

The relative growth rate of baroclinic waves can also be compared by seeing how often the EKE-BW of each experiment reaches the amplitude of approximately 52.5 m² s⁻². It is about 132 h for both EXP00 and EXP20, by which time mature gravity waves can clearly be identifiable in both EXP00 and EXP20 (details later). Increasingly shorter time is needed to reach the same EKE-BW amplitude for other experiments with more moisture (e.g., 129 h for EXP40, 126 h for EXP60, 121 h for EXP80, and 116 h for EXP100). Following Badger and Hoskins (2001), an average growth rate of the baroclinic waves in terms of EKE is defined as

$$\sigma = \frac{\ln\left(\frac{EKE_t}{EKE_0}\right)}{t}, \quad (2)$$

where EKE_0 and EKE_t are, respectively, the EKE-BW at initial time 0 and t , where t is the above-mentioned time when the EKE-BW reaches approximately 52.5 m² s⁻² in each experiment. The average growth rates of baroclinic waves σ are 0.0947 s⁻¹ for EXP00, 0.0953 s⁻¹ for EXP20, 0.0974 s⁻¹ for EXP40, 0.100 s⁻¹ for EXP60, 0.104 s⁻¹ for EXP80, and 0.109 s⁻¹ for EXP100. Figure 1b further compares the meridional variation of zonal maximum CAPE at the hour that the EKE-BW in each experiment exceeds this threshold magnitude. For both EXP00 and EXP20, there is no CAPE over the entire domain, although EXP20 exhibits a characteristic of conditional instability from the southern frontal system to the northern cyclone center, which corresponds to a negative vertical gradient of saturation equivalent potential temperature (not shown). EXP40 and EXP60 have peak CAPE values of 90.2 and 259.1 J kg⁻¹, respectively. EXP80 has the highest peak CAPE of 582.2 J kg⁻¹. The highest CAPE in EXP100 is 508.4 J kg⁻¹, which is slightly smaller than in EXP80, but the areal extent is

larger in EXP100. Overall, the CAPE values in all of these experiments are small to moderate, likely due to the efficient convective triggering mechanism of the large-scale baroclinic waves.

Other variables related to moist processes are also investigated in all experiments (not shown), including latent heating, total cloud mixing ratio, and 1-h precipitation. For example in EXP100, the noticeable latent heating release starts from around 55 h, and the apparent increase in total cloud mixing ratio and 1-h precipitation can be seen from around 60 h. For EXP20, there is almost no precipitation during 50–140 h, although a somewhat small but nonzero latent heating release and total cloud mixing ratio begin at around 103 h. These variables are all zero in EXP00 by design.

Figures 3–5 show the 1-km temperature, 8-km horizontal wind, and 12-km horizontal divergence at selected times that further display that evolution of the baroclinic waves in different experiments (along with an overview of different modes of gravity waves at different stages of the baroclinic development; details in section 4). More specifically, Fig. 3 collects the baroclinic structures in the same experiment of EXP20 valid at 116, 132, 148, and 164 h. Figure 4 compares these variables in EXP00, EXP40, EXP60, and EXP100 at 132, 129, 126, and 116 h, respectively, with EXP20 at 132 h in Fig. 3b. These are the times by which the EKE-BW in these experiments reach similar amplitudes (start of the mature gravity wave stage in EXP00; refer to Fig. 2a). Figure 5 provides those at 116 h in EXP00, EXP40, EXP60, and EXP80, which is the approximate time that the shorter-scale gravity wave modes first appear in EXP20 (Fig. 3a). As in Z04, the life cycle of the moist baroclinic waves develops from small-amplitude synoptic-scale 3D PV perturbations seeded at the 2D jet (not shown). As time goes by, an incipient cyclone has developed as an elongated 8-km jet streak is found above

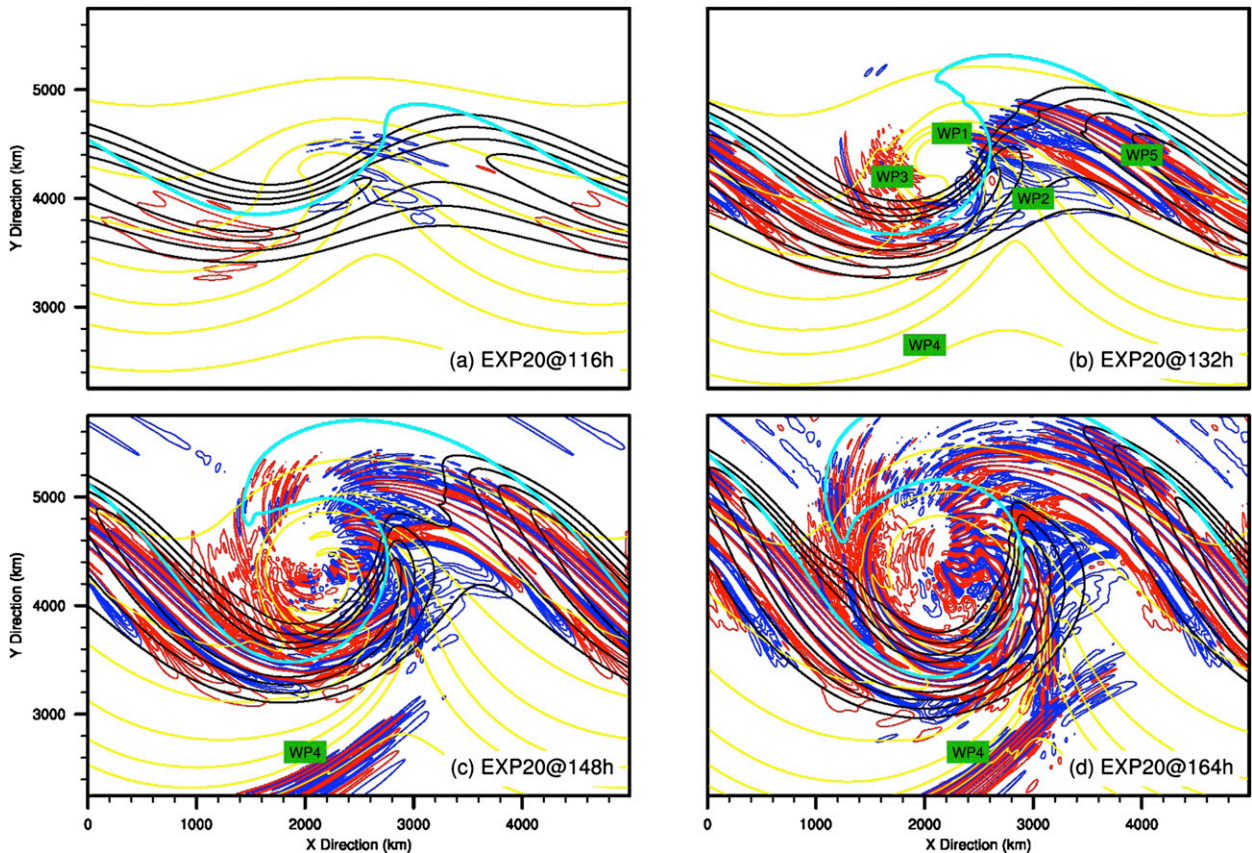


FIG. 3. Simulated 1-km temperature (yellow lines; $\Delta = 5$ K), 8-km horizontal wind (black lines; contours at 40, 45, 50, and 55 m s^{-1}), and 12-km horizontal divergence (blue lines, positive; red lines, negative; $\Delta = 2.0 \times 10^{-6} \text{ s}^{-1}$; range within $\pm 1.2 \times 10^{-5} \text{ s}^{-1}$; zero value omitted) in EXP20 at (a) 116, (b) 132, (c) 148, and (d) 164 h. The turquoise lines denote the 7-km dynamic tropopause where potential vorticity equals 1.5 PVU . WP1–WP5 are marked.

the surface frontal systems (e.g., Figs. 3a and 5a). The tropopause, accompanied with the strengthening upper-level jet streak, begins to descend toward the lower troposphere. The synoptic-scale structure at the time that mature gravity waves appear in EXP00 (e.g., Figs. 3b and 4) is characterized by a well-developed upper-level undulated baroclinic jet, with the surface featuring a continuously deepening surface cyclone, strengthening cold and warm fronts, and the emergence of an occluded front as part of a “T-bone” structure (Shapiro and Keyser 1990). Broadly speaking, the evolution of simulated moist baroclinic waves is qualitatively similar to the life cycle of CNTL in Z04 (except for an increasingly faster growth rate in experiments with increasingly larger moisture content) (e.g., cf. our Figs. 3b and 4 with Z04’s Figs. 2d–4d). Noticeable shape differences among all runs in surface temperature and the upper-level jet can be found at this stage (Figs. 3b and 4), even though they should share similar EKE-BW values. Note that the 12-km divergence in Figs. 3–5 suggests systematic signals of gravity waves during the evolution of moist baroclinic

waves that will be explored in detail in the following sections.

4. Characteristics of simulated mesoscale gravity waves

a. Overview

Similar to EKE-BW [Eq. (1) in section 3], the mesoscale gravity wave component of EKE (EKE-GW) is calculated by applying another band-pass filter to extract three-dimensional velocity perturbations with horizontal wavelengths from 50 to 600 km. Figure 2b shows the time change of EKE-GW during 50–140 h in each experiment. There is little difference in EKE-GW among all experiments before 80 h, and no apparent difference between EXP00 and EXP20 even before 110 h. Generally speaking, the growth of EKE-GW in EXP100 is much faster than any experiment with reduced or zero initial moisture content. To be specific, at the stage when all experiments reach similar EKE-BW

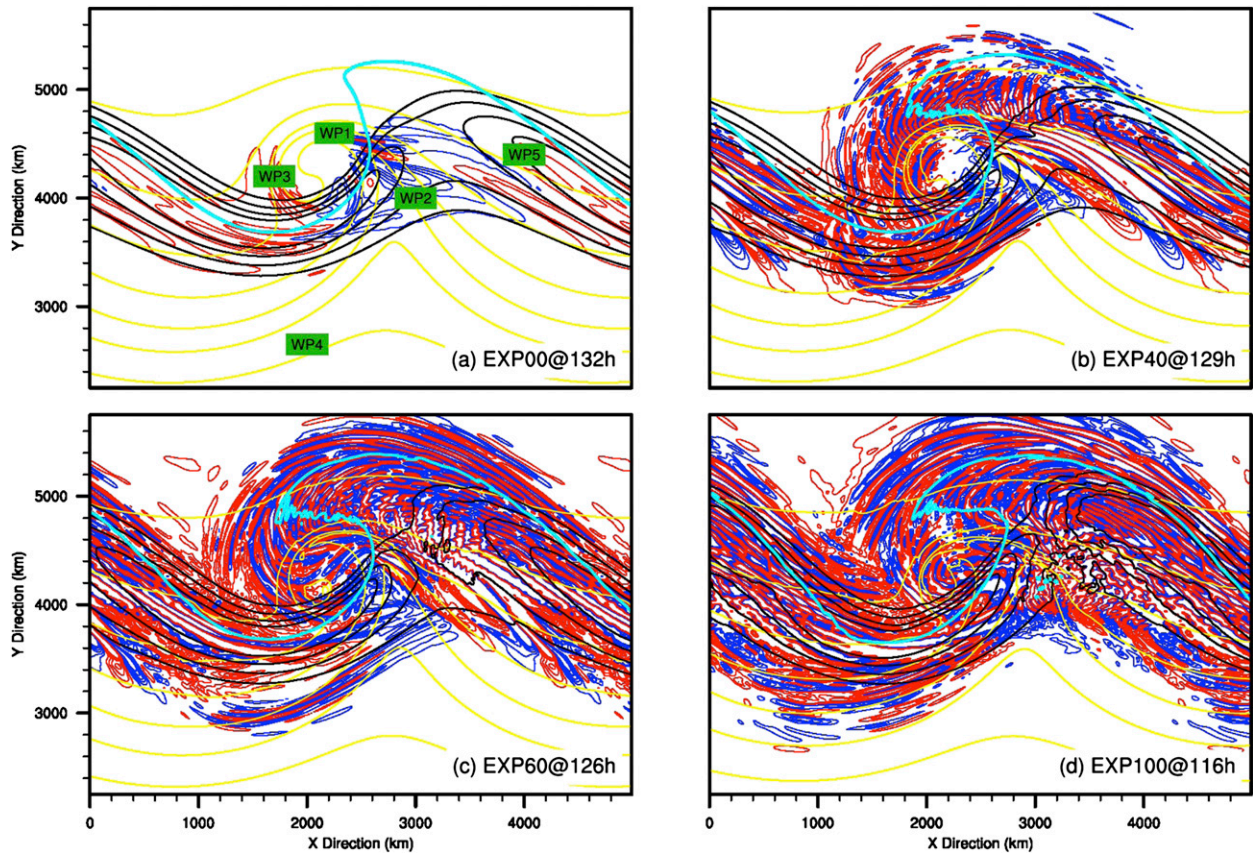


FIG. 4. As in Fig. 3, but for (a) EXP00 at 132 h, (b) EXP40 at 129 h, (c) EXP60 at 126 h, and (d) EXP100 at 116 h.

values of about $52.5 \text{ m}^2 \text{ s}^{-2}$, EKE-GW is greater with a faster baroclinic wave growth rate (e.g., $0.33 \text{ m}^2 \text{ s}^{-2}$ in EXP00, $0.45 \text{ m}^2 \text{ s}^{-2}$ in EXP20, $0.62 \text{ m}^2 \text{ s}^{-2}$ in EXP40, $0.81 \text{ m}^2 \text{ s}^{-2}$ in EXP60, $0.88 \text{ m}^2 \text{ s}^{-2}$ in EXP80, and $1.61 \text{ m}^2 \text{ s}^{-2}$ in EXP100). Accordingly, compared to EKE-BW, it takes less time for each experiment to reach a similar amplitude of EKE-GW at 132 h in EXP00 (e.g., 129 h in EXP20, 122 h in EXP40, 116 h in EXP60, 109 h in EXP80, and 101 h in EXP100). As in Z04 and LZ08, this research focuses on the upper-tropospheric and lower-stratospheric horizontal velocity divergence (as a measure of flow imbalance and/or gravity waves).

The evolution of the horizontal velocity divergence at 12 km during the dry baroclinic wave life cycle in EXP00 is also examined. Given that the initial conditions of the BW are nonlinearly balanced, there is only a weak (albeit growing) divergence signal before 70 h (not shown). Consistent with Keyser and Shapiro (1986), the lower-stratospheric divergence flow in EXP00 at 110–116 h (Fig. 5a) features a typical pattern with convergence upstream of the trough and divergence downstream of the trough. As in Z04 (his Fig. 4d), the divergence in EXP00 at the mature stage of the gravity waves (Fig. 4a)

is characterized by mesoscale perturbations with various horizontal wavelengths of less than 500 km, especially in the jet exit region downstream of the trough and above the occluded frontal systems. It is worth mentioning that mesoscale variations with rather weak amplitude can also be identified in the jet entrance region upstream of the trough and along the surface warm front (although not highlighted, they are also present in the simulation of Z04).

The evolution of the 12-km horizontal velocity divergence in EXP20 (Fig. 3) is broadly similar to that in EXP00. Despite the general resemblance, EXP20 differs from EXP00 in several key respects. First, at 110–116 h (cf. Figs. 5a and 3a), gravity waves with shorter-scale horizontal wavelengths ($\sim 50\text{--}60$ km) in EXP20 emerge above the surface frontal systems to the north of the jet exit region, which are not apparent in EXP00. Second, at the mature gravity wave stage (cf. Figs. 4a and 3b), the amplitude of the mesoscale variations in the jet entrance region upstream of the trough is much stronger in EXP20 than EXP00 (peak amplitude of divergence $\sim 9.1 \times 10^{-6} \text{ s}^{-1}$ versus $\sim 4.1 \times 10^{-6} \text{ s}^{-1}$ in the southern part; $\sim 2.3 \times 10^{-6} \text{ s}^{-1}$ versus $\sim 1.2 \times 10^{-6} \text{ s}^{-1}$ in the

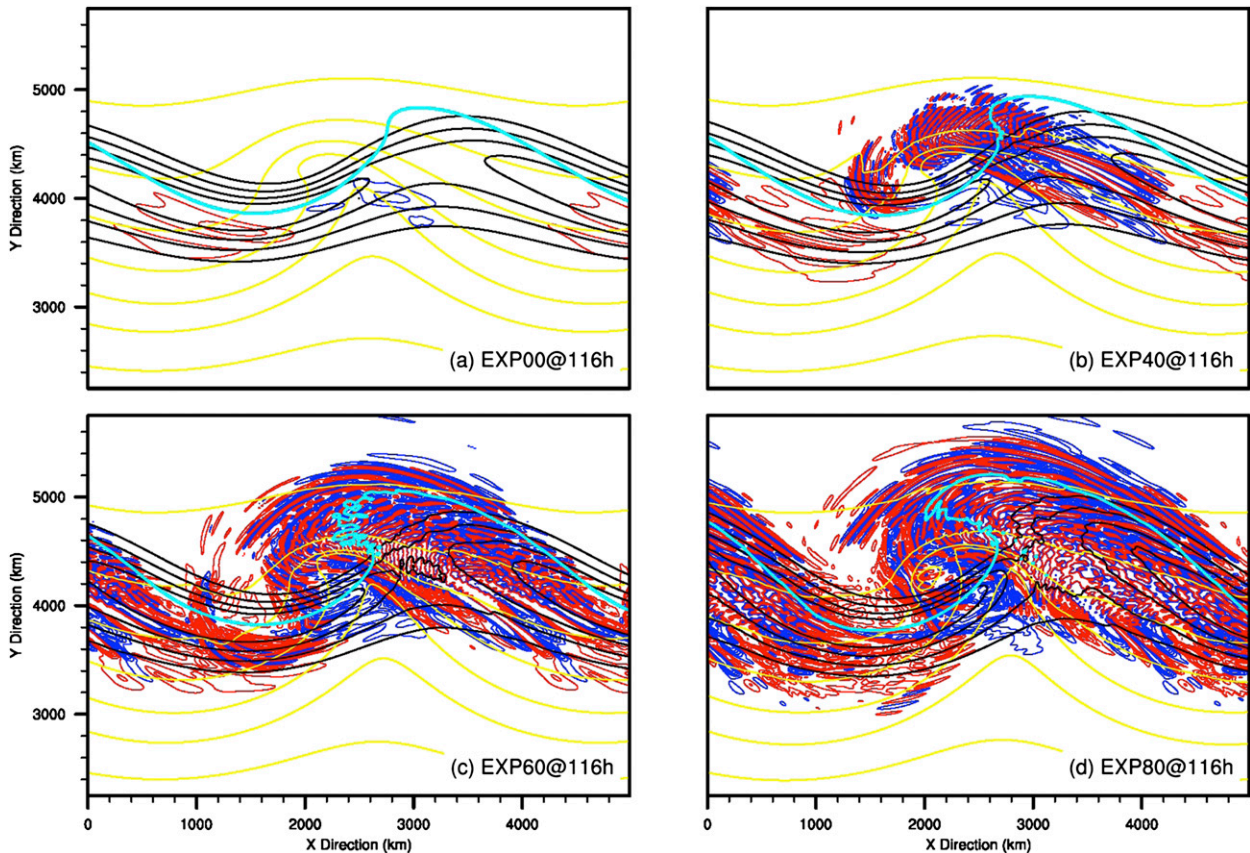


FIG. 5. As in Fig. 3, but for (a) EXP00, (b) EXP40, (c) EXP60, and (d) EXP80 at 116 h.

northern part). Also at this stage (cf. Figs. 4a and 3b), there exists a noticeable pattern distinction between the bended shorter-scale gravity wave to the west of the cyclone center in EXP20 and that in EXP00.

With increasingly higher initial moisture content, the 12-km horizontal velocity divergence manifests more mesoscale perturbations associated with the faster growth of a baroclinic jet-front (cf. Figs. 4a and 3a and also Figs. 4b–d). For example, in EXP40 at 129 h (Fig. 4b), there exist additional shorter-scale variances, which appear to be perpendicular to 1-km potential temperature along the occluded/warm fronts. Furthermore, the 12-km horizontal velocity divergence in both EXP60 and EXP100 differs drastically from that in EXP00 or that in EXP20 (Figs. 4c,d). First, gravity waves with shorter-scale horizontal wavelengths are apparent as early as 72 h in EXP100 (details later) with a rather weak synoptic-scale disturbance (e.g., $\text{EKE-BW} = 1.84 \text{ m}^2 \text{ s}^{-2}$ at 72 h versus $\text{EKE-BW} = 55.68 \text{ m}^2 \text{ s}^{-2}$ at 116 h), while no gravity wave signal with similar characteristics is seen in either EXP00 or EXP20 at the same EKE-BW value. Second, the lower-stratosphere divergence in EXP100 at 116 h (Fig. 4d) manifests shorter-scale wave signatures filling the whole

region of the baroclinic jet. By contrast, it is much easier to classify each shorter-scale or intermediate-scale wave packet with the divergence fields in EXP00 (Fig. 4a) and in EXP20 (Fig. 3b) at 132 h, both of which reach a mature-phase amplitude of EKE-BW that is similar to that in EXP100 at 116 h.

b. Wave identification

In this section, we will examine in detail the characteristics of several identifiable gravity wave packets in the upper troposphere and lower stratosphere. As noted above, both shorter-scale and intermediate-scale wave packets are much easier to identify in EXP00 and EXP20. Wave identification is thus mainly centered on the comparison between these two experiments, complementary to Z04 and Wang and Zhang (2007). In addition, this section also introduces a potentially new mode of gravity waves observed in the early period of the moist baroclinic life cycle in both EXP20 and EXP100. Nevertheless, characterizations of each of the many other modes of gravity waves that existed in full or other moist experiments are beyond the scope of the current study.

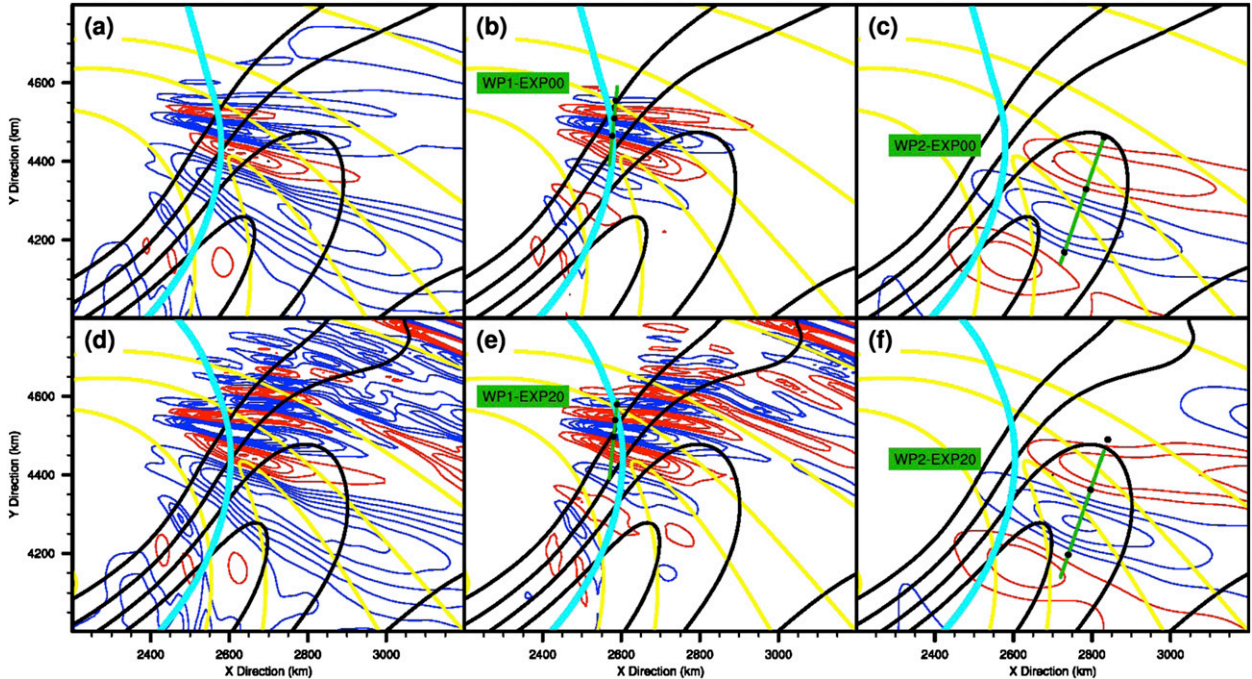


FIG. 6. Examples of WP1 and WP2 in (a)–(c) EXP00 and (d)–(f) EXP20 at 132 h. Contours follow Fig. 3, except that (b),(e) shorter- and (c),(f) intermediate-scale divergence are used to separate WP1 and WP2. The green lines (black dots) represent the approximate cross sections (locations) used to estimate wave characteristics. WP1-EXP00, WP2-EXP00, WP1-EXP20, and WP2-EXP20 are marked.

Table 1 summarizes the gravity wave characteristics for the six highlighted gravity wave modes in EXP00, EXP20, and EXP100, which will be identified and introduced in this section. The calculation of wave characteristics in Table 1 generally follows Table 3 in Wang and Zhang (2007). Assuming the wave vectors are perpendicular to the phase lines, the horizontal wavelengths λ_h and vertical wavelengths λ_z are estimated by measuring the neighboring phase lines that cover both maximum and minimum perturbation at or near the selected level. The intrinsic frequency of the gravity waves Ω is then derived based on the dispersion for plane waves [e.g., Eq. (23) in Fritts and Alexander (2003)]:

$$\Omega^2 = \frac{N^2 K_h^2 + f^2(m^2 + \alpha^2)}{K_h^2 + m^2 + \alpha^2}, \quad (3)$$

where $K_h = 2\pi/\lambda_h$ and $m = 2\pi/\lambda_z$ are the horizontal and vertical wavenumbers, respectively; N is the buoyancy frequency averaged over one horizontal and vertical wavelength; the Coriolis parameter $f = 10^{-4} \text{ rad s}^{-1}$; and $\alpha = 1/4H^2$, where scale height H is 7500 m. Assuming waves travel against background flow horizontally, upward-propagating gravity waves with downward-propagating phase should have negative K_h and m when

Ω is positive. Therefore, the theoretical intrinsic horizontal phase speed c_i , given by Ω/K_h , is negative. To verify c_i derived from the dispersion relation, the observed intrinsic horizontal phase speed C_{io} can also be estimated by $C_d - U_h$, where C_d is the ground-based phase speed over a 2-h period centered on the selected time and U_h is the wind speed along wave vectors averaged over one horizontal and vertical wavelength.

Figure 6 shows the examples of the first two gravity wave modes (WP1 and WP2; also marked in Figs. 4a and 3b) in EXP00 and EXP20, which includes the northward-propagating shorter-scale and intermediate-scale wave packets (Figs. 6a,d) pronounced in the exit region of the upper-tropospheric jet. Similar to Fig. 2 in LZ08, a 2D Fourier decomposition is also employed to decompose the divergence field into the shorter-scale component with wavelength between 50 and 200 km, and the intermediate-scale component with wavelength between 200 and 600 km. WP1-EXP00 (Fig. 6b) represents the shorter-scale wave packets on the left side of the immediate jet exit region in EXP00, and WP1-EXP20 (Fig. 6e) represents those in EXP20. Similarly, WP2-EXP00 (Fig. 6c) represents the intermediate-scale wave packets in the immediate exit region of the jet streak in EXP00, and WP2-EXP20 (Fig. 6f) represents those in EXP20. According to Table 1, the intrinsic frequencies of WP1 are roughly 4 times the Coriolis

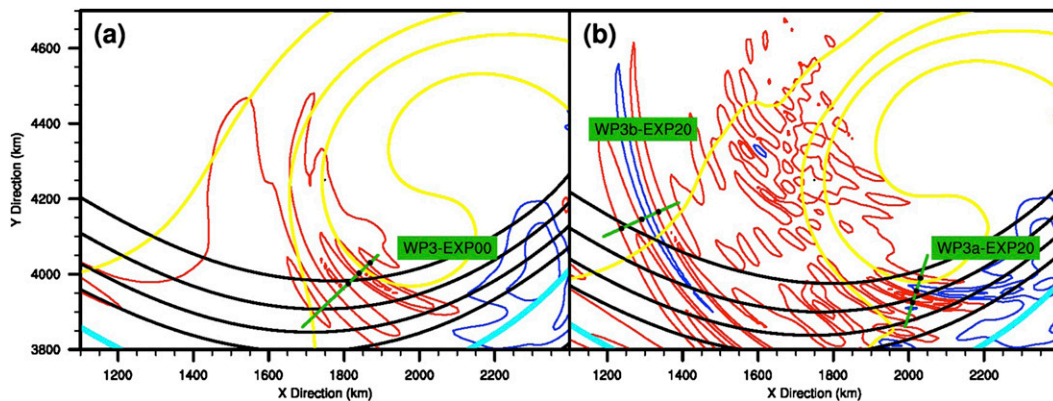


FIG. 7. As in Fig. 6, but for WP3 in (a) EXP00 and (b) EXP20 at 132 h. WP3-EXP00, WP3a-EXP20, and EXP3b-EXP20 are marked.

parameter, much higher than the low intrinsic frequencies of WP2 ($\sim 2f$). WP1 and WP2 have distinctively different wave characteristics, even though they may share similar locations or background flows at 12 km. This result is generally consistent with LZ08.

Figure 7 shows the examples of the third gravity wave mode (WP3; also marked in Figs. 4a and 3b) highlighted in the study. WP3-EXP00 (Fig. 7a) represents the shorter-scale wave packets over the deep trough region above the jet in EXP00, and WP3a-EXP20 (Fig. 7b) represents those in EXP20. Unlike the comparison in WP1 and WP2 between EXP00 and EXP20, there are noticeable differences in wave characteristics and their locations between WP3-EXP00 and WP3a-EXP20. However, both of these simulations behave as bended shorter-scale wave packets almost parallel with the surface occluded front to the south of the cyclone center. Also, they both share remarkably high intrinsic frequencies, with 11–15 times the Coriolis parameter. A seemingly new gravity wave mode in EXP20, named WP3b-EXP20 here, is also shown to the west of the cyclone center. The generation and propagation of WP3b-EXP20 will be further described in section 5c.

The fourth gravity wave mode (WP4) represents the shorter-scale wave packets located far to the south of the jet right above the surface cold front (its approximate location is marked in Figs. 3b and 4a but the wave amplitude at this level/time is below the lowest contour values of $\pm 2.0 \times 10^{-6} \text{ s}^{-1}$ in horizontal divergence; WP4 is clearly identifiable and also marked at later times in Figs. 3c and 3d). In both EXP00 and EXP20 at 132 h, WP4 has a horizontal wavelength of about 95 km and a vertical wavelength of about 2.0 km at 10 km. They have intrinsic frequencies of approximately 2–3 times the Coriolis parameter.

Figure 8 shows the examples of the fifth gravity wave mode (WP5; also marked in Figs. 4a and 3b) in EXP00

and EXP20, which refer to the wave packets from the jet exit region in the ridge down to the jet entrance region in the trough. For each run, WP5 consists of two wave patterns with separate phase-line tilting angles in the selected cross section (Figs. 8b,d). On the one hand, WP5s-EXP00 (Figs. 8a,b) represents the southern part (location is about 300–1000 km in the vertical cross section) of wave packets (WP5s) located just above and almost parallel with the tropopause at 132 h in EXP00, while WP5s-EXP20 (Figs. 8c,d) represents those at 132 h in EXP20. On the other hand, WP5n-EXP00 (Figs. 8a,b) represents the northern part (location is about 1000–1400 km in the vertical cross section) of wave packets (WP5n) located about 2 km above the tropopause at 132 h in EXP00, while WP5s-EXP20 at 132 h (Figs. 8c,d) represents those at 132 h in EXP20. According to Table 1, both WP5s and WP5n have relatively low intrinsic frequencies. The intrinsic frequencies of WP5n are over 3 times the Coriolis parameter, higher than the intrinsic frequencies of WP5s ($\sim 1.2\text{--}1.3f$). Accordingly, the phase line of WP5n is steeper than that of WP5s in the vertical cross section. The wave characteristics of both WP5s and WP5n in EXP20 are generally similar to those in EXP00 (Table 1). However, there are noticeable differences between EXP00 and EXP20 for WP5: in terms of wave amplitude, the divergence related to WP5 in EXP20 is much stronger; in terms of structure, WP5 between the jet exit region and the jet entrance region tend to approach each other in EXP00, while they are nearly connected as one wave packet in EXP20. Note that there exists strong divergence from about 3 to 9 km below the tropopause in EXP20 while no corresponding signal is shown in EXP00. The evolution of WP5 will be discussed further in section 5b.

Figure 9 shows the examples of the sixth gravity wave mode (WP6) in EXP20 and EXP100, which refers to the upper-level shorter-scale wave packets before WP1–WP5

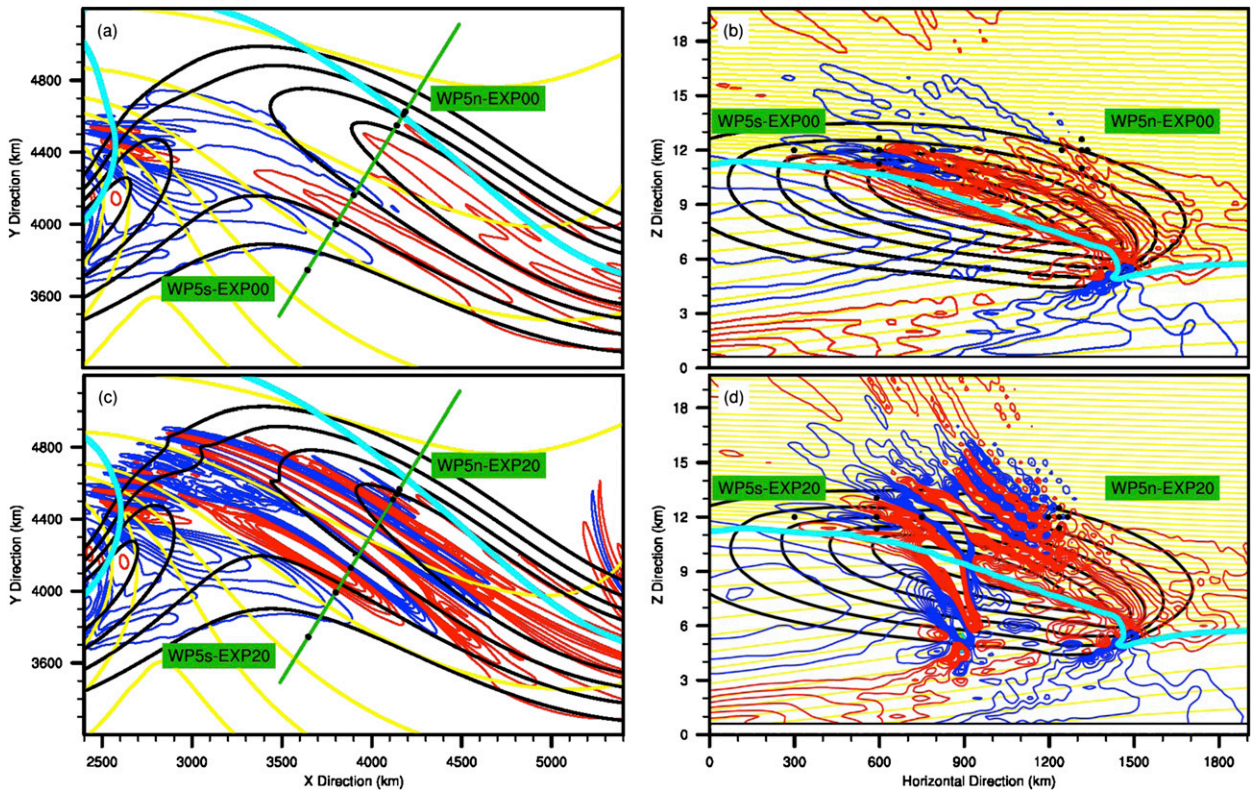


FIG. 8. As in Fig. 6, but for WP5 in (a) EXP00 and (c) EXP20 at 132 h. (b),(d) The corresponding vertical cross sections used to estimate wave characteristics: black lines denote horizontal velocity ($\Delta = 5 \text{ m s}^{-1}$ from 30 to 65 m s^{-1}), yellow lines denote potential temperature ($\Delta = 5 \text{ K}$), blue and red lines denote horizontal divergence (blue lines, positive; red lines, negative; $\Delta = 1.0 \times 10^{-6} \text{ s}^{-1}$), and light turquoise thick lines denote the location of the tropopause where potential vorticity equals 1.5 PVU. WP5s-EXP00, WP5n-EXP00, WP5s-EXP20, and WP5n-EXP20 are marked.

become mature. The horizontal wavelength of WP6 are only about 5–6 times the horizontal resolution in the experiments, so the amplitude of WP6 may be sensitive to and determined by the model horizontal resolution (details in section 6c). While holding the shortest horizontal wavelength among all the gravity wave modes, WP6 has rather high intrinsic frequencies with about 9–12 times the Coriolis parameter. WP6 in EXP20 and EXP100 are both generated after the release of latent heating. WP6 is seen in EXP20 at 110 h (Figs. 9a,b) when frontal systems have developed, while WP6 in EXP100 is observed much earlier (at 72 h), when there is no systematic frontal system. The generation of WP6 will be given in section 5a.

5. Evolution of simulated mesoscale gravity waves

Among the six listed gravity wave modes in section 4b, WP1–WP5 in EXP00 have a corresponding resemblance in Z04, while WP1–WP4 are the primary focus in LZ08. According to the ray-tracing analysis in LZ08, WP1 (their Fig. 4) may originate from both the upper-tropospheric

jet and the surface frontal system. WP2 (their Fig. 7) originates from the upper-tropospheric jet–front system where there is maximum imbalance, although a contribution from the surface fronts cannot be completely ruled out. WP3 (their Fig. 4) and WP4 (not shown in LZ08) are almost certain to initiate from the surface frontal system. This section will continue to investigate the generation and propagation of other simulated gravity wave modes.

a. Potential source mechanism for WP6

To investigate the source mechanism for WP6-EXP20 at 110 h, its horizontal evolution is demonstrated at 12 km in Fig. 10. At 102 h (Fig. 10a), WP6 cannot be identified when no latent heating is released. At 104 h (Fig. 10b), WP6 is too weak to identify with selected divergence contour levels, since latent heating has been released for only about 2 h in EXP20. However, approximately one to two waves with rather weak amplitude emerge along the selected cross section at 9–12 km (not shown), above a rather weak convective disturbance associated with latent heating. At 106 h, a weak

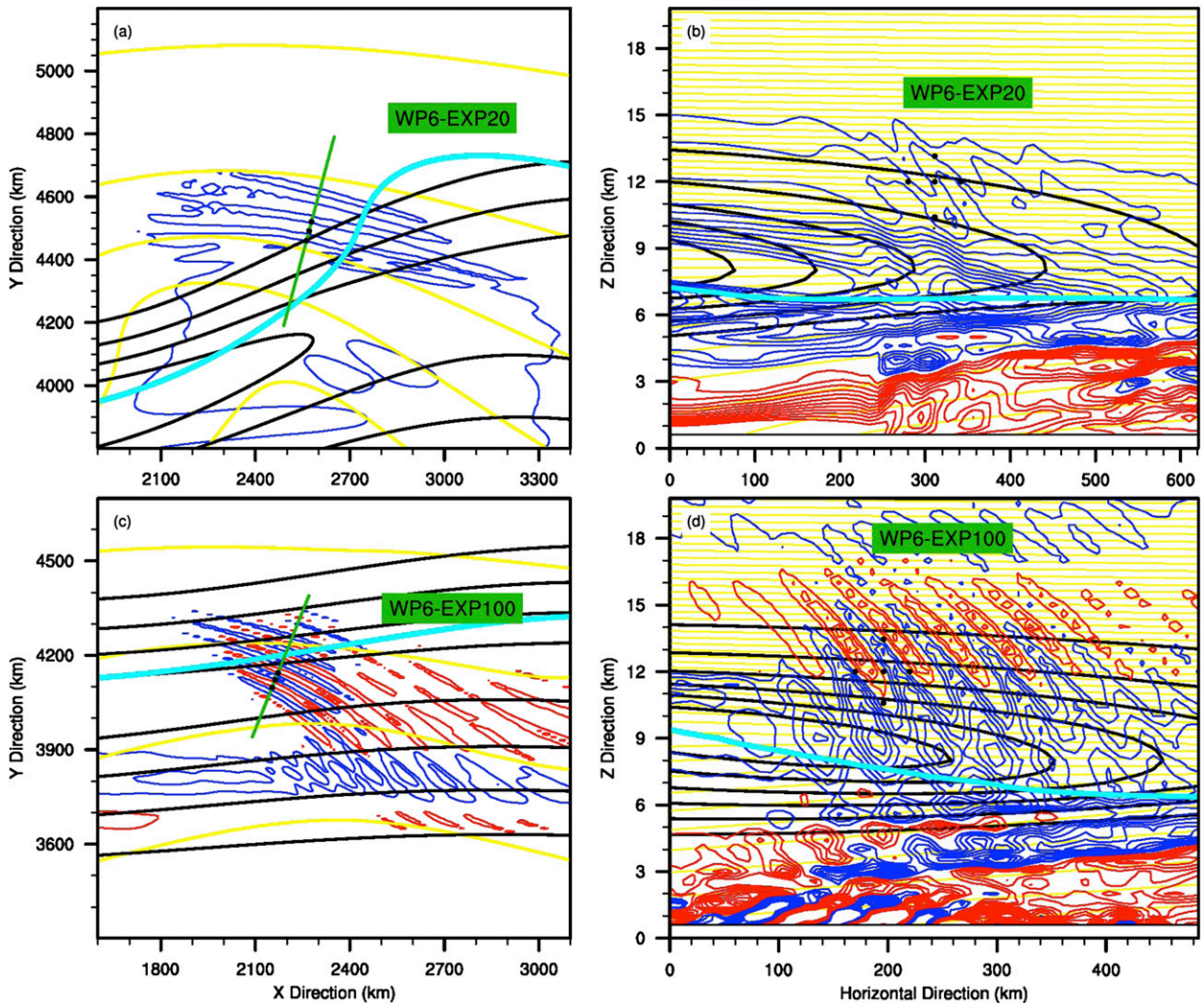


FIG. 9. As in Fig. 8, but for WP6 in (a),(b) EXP20 at 110 h and (c),(d) EXP100 at 72 h. WP6-EXP20 and WP6-EXP100 are marked.

WP6 emerges at 12 km (Figs. 10c) while approximately three to four waves with weak amplitude can also be observed above the convection viewed from its vertical structure (not shown). At 108 h (Fig. 10d), the synoptic-scale divergence is overlaid with identifiable high-frequency WP6 at 12 km, and the amplitude of WP6 gets much stronger. In brief, as the block of latent heating rate grows over the frontal boundary, WP6 develops at the same time above the continuously growing low-level convective disturbance. Most importantly, the horizontal phase line of WP6 at 12 km matches the contour of the vertically averaged positive-only latent heating rate almost perfectly, including its location, orientation, and timing. Considering all the above-mentioned factors, convection may be the most likely source mechanism for WP6. Note that the current study has no attempt to investigate the exact type of convection, and all latent

heating release is loosely attributed to convection associated with moist processes.

b. Evolution of WP5

Figure 11 demonstrates the horizontal evolution of WP5 with 12-km horizontal velocity divergence from 102 to 130 h in both EXP00 and EXP20. The vertically averaged positive-only latent heating rate is also given in Fig. 11. During 110–114 h in EXP00 (Figs. 11a,b), only a weak obscure wave pattern exists in the jet exit and entrance regions at 12 km. During 118–122 h in EXP00 (Figs. 11c,d), a weak WP5 signal starts to approach from the jet entrance region toward the jet exit region (e.g., the red wavelike divergence contours barely touch the short-dashed line at 122 h); the intermediate-scale WP2 emerges in the jet exit region. During 126–130 h in EXP00 (Figs. 11e,f), WP5 continues to approach the jet

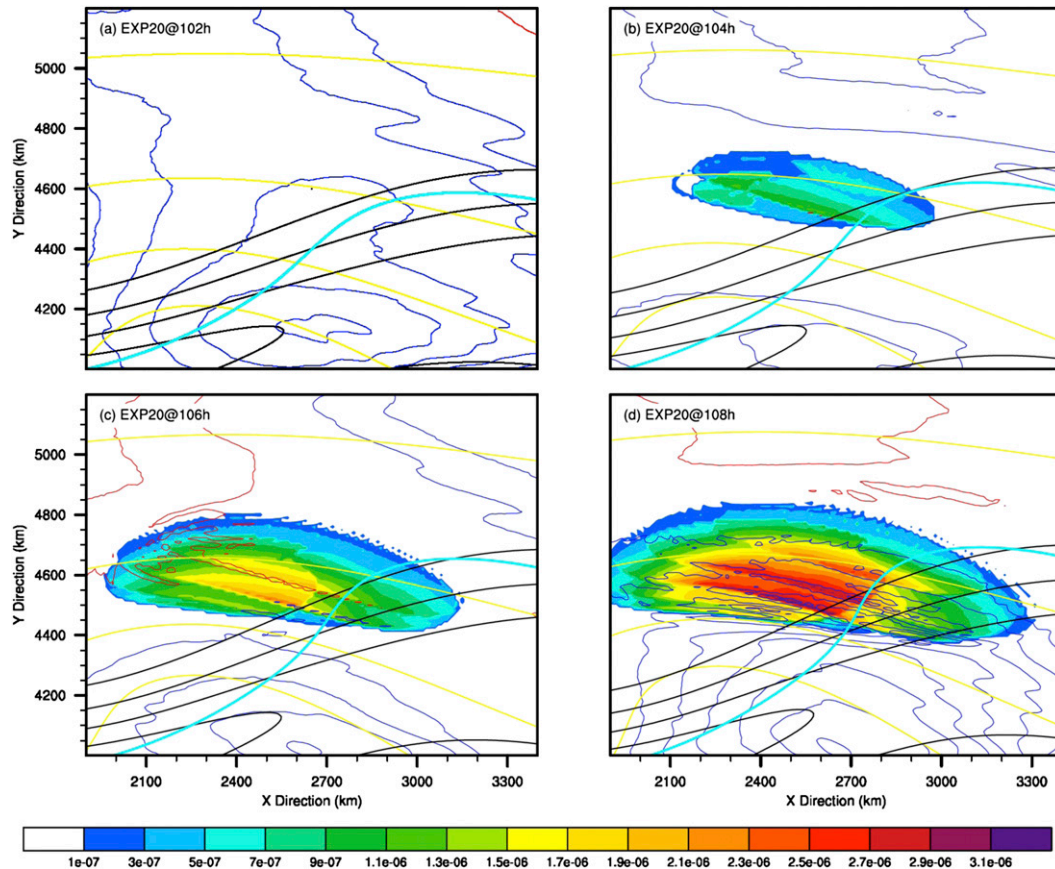


FIG. 10. The horizontal evolution of WP6 every 2 h from (a) 102 to (d) 108 h in EXP20. Contours follow Fig. 3, except that $\Delta = 5.0 \times 10^{-7} \text{ s}^{-1}$ for 12-km horizontal divergence. The shading denotes the vertically averaged positive-only latent heating rate (K s^{-1}).

exit region, the amplitude of WP2 is strengthened, and the shorter-scale WP1 is established on the left side of the immediate jet exit region. Note that WP5s and WP2 in EXP00 are almost connected at 130 h. Since the most important difference between EXP00 and EXP20 lies in the release of latent heating from about 103 h, the comparison between EXP00 and EXP20 reveals the role of latent heating in the WP5 evolution for EXP20. At 102 h (not shown), EXP00 and EXP20 share almost the same pattern in 12-km divergence since there is no latent heating in both runs. At 106 h (not shown), the difference in 12-km divergence between EXP00 and EXP20 is still rather weak since latent heating has been released for only about 3 h in EXP20. At 110 h (cf. Figs. 11a and 11g), one can identify WP6 in EXP20 over the area with a nonzero latent heating rate; no apparent wave difference between EXP00 and EXP20 is shown along the short-dashed line. During 110–118 h in EXP20 (Figs. 11g–i), the signal of WP6 is not stable at 12 km. It is worth mentioning that there is no corresponding resemblance of WP6 in EXP00, even after several hours

with greater baroclinic instability. This again suggests that local convection associated with a latent heating release may be the potential source mechanism for the generation of WP6 (section 5a). Note that there are noticeable wave differences along both the long- and short-dashed lines at 118 h (cf. Figs. 11c and 11i). This suggests that wave differences may travel from upstream localized convection toward a downstream jet entrance region. During 122–130 h (cf. Figs. 11d,f and 11j,l), wave packets in EXP20 between the jet exit region and the jet entrance region are gradually connected as one wave packet, and wave differences between EXP00 and EXP20 within this area become more and more apparent.

Figure 12 continues to demonstrate the vertical evolution of the horizontal velocity divergence in EXP00 and EXP20 along the long-dashed line in Fig. 11. Again, the positive-only latent heating rate is given in Fig. 12. During 110–114 h in EXP00 (Figs. 12a,b), no apparent wave is identified in the stratosphere, although the low-level divergence signal is strong due to the vertical motion

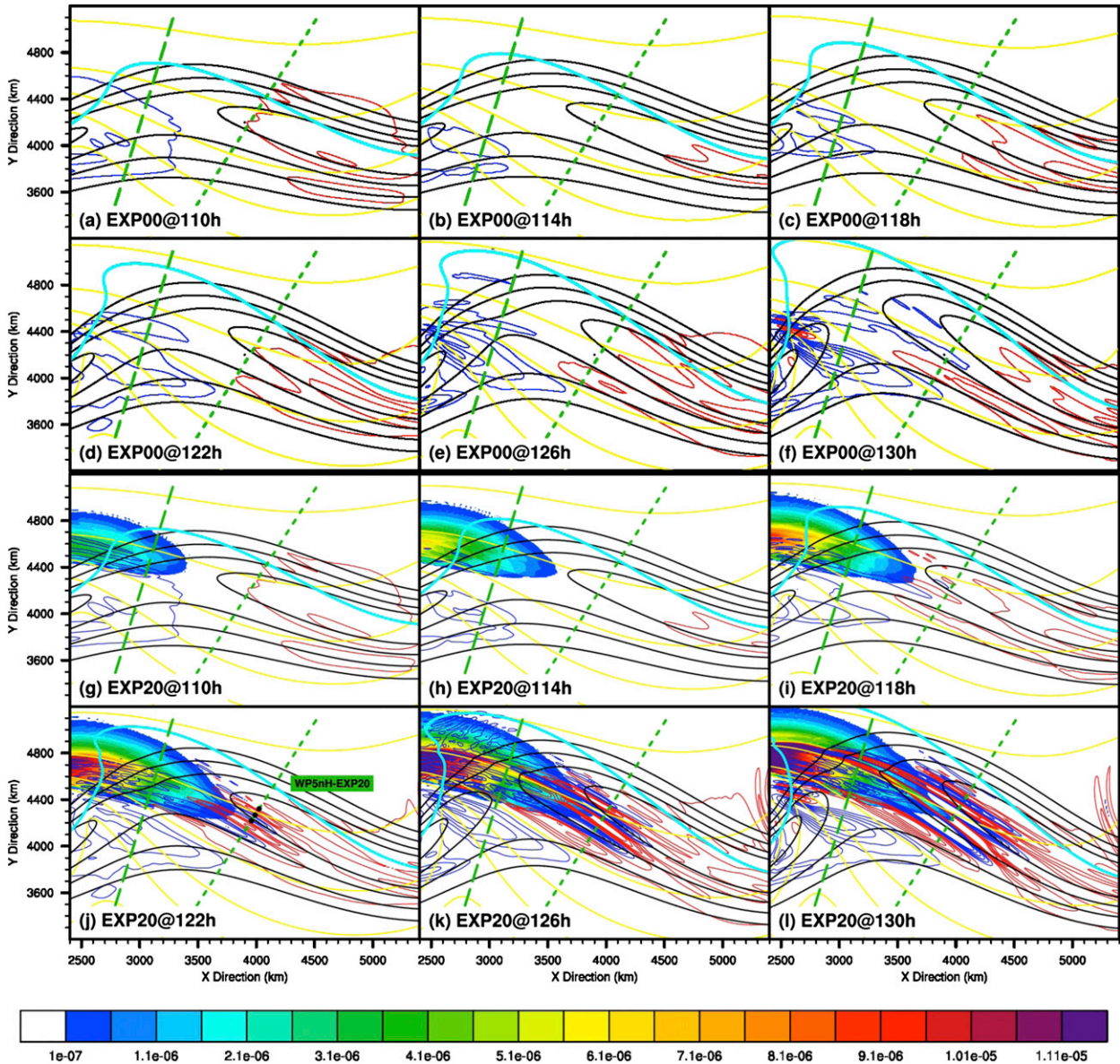


FIG. 11. Horizontal evolution of WP5 every 4 h from 110 to 130 h in (a)–(f) EXP00 and (g)–(l) EXP20. Contours follow Fig. 3. The shading denotes the vertically averaged positive-only latent heating rate (K s^{-1}). The green long-dashed and short-dashed lines represent the selected cross sections in Figs. 12 and 13. WP5nH-EXP20 is marked.

associated with surface frontal systems. During 118–130 h in EXP00 (Figs. 12c–f), the intermediate-scale WP2 near 12 km emerges from about 118 h and its amplitude is strengthened over time. For the comparison between EXP00 and EXP20, the cross section shows no obvious distinction during 102–106 h (not shown). During the next 8 h (Figs. 12a,b and 12g,h), high-frequency WP6s are propagating from the low-level disturbance collocated with the low-level latent heating release up to the stratosphere near 20 km. At 118 h in EXP20 (Fig. 12i), it appears that there is a concurrence of three gravity

wave modes along the same cross section. Weak WP2 is located within about 0–900 km (of the cross section; same below) near 12–14 km, strong WP5nL-EXP20 (marked) is located within about 1100–1500 km near 8–10 km, and another clear wave mode is located within about 900–1200 km near 12–20 km (partially within the sponge layer). During 122–130 h in EXP20 (Figs. 12j–l), three above-mentioned gravity wave modes are propagating northward with each other; the amplitudes of WP2 and WP5nL-EXP20 are gradually enhanced. Note that the amplitude of WP2 at 130 h in EXP20 is greater

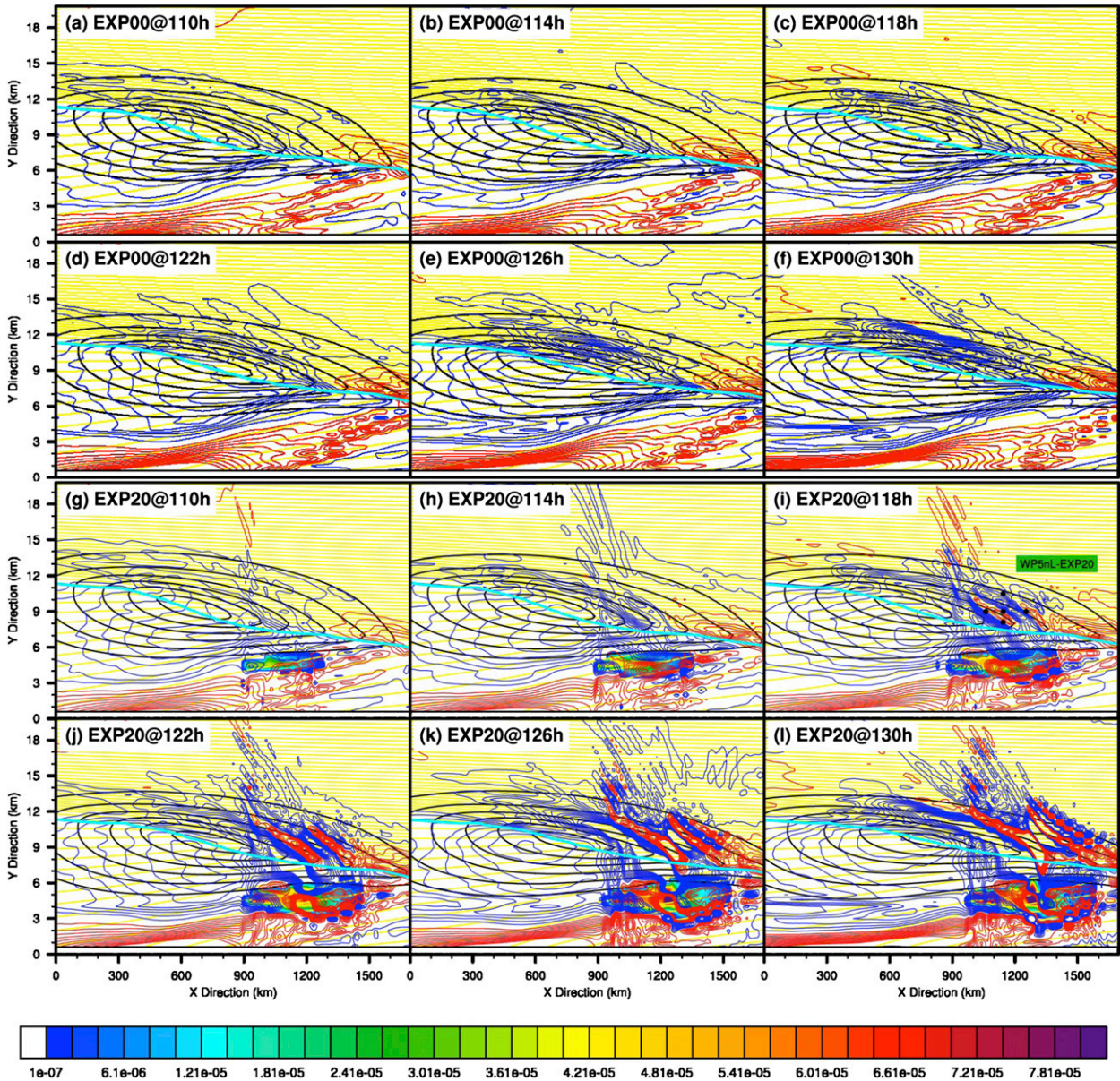


FIG. 12. Vertical evolution every 4 h from 110 to 130 h in (a)–(f) EXP00 and (g)–(l) EXP20, viewed along the vertical cross section of the green long-dashed line in Fig. 11. Contours follow Fig. 8b. The shading denotes the vertically averaged positive-only latent heating rate ($K s^{-1}$). WP5nL-EXP20 is marked.

than that in EXP00, although there is no apparent difference in their wave characteristics.

In addition to the analysis along the long-dashed line, Fig. 13 gives another vertical view of WP5’s evolution along the short-dashed line. During 110–114 h in EXP00 (Figs. 13a,b), weak WP5s can be observed above the tropopause while no apparent WP5n is identified. During 118–130 h in EXP00 (Figs. 13c–f), both WP5s and WP5n gradually become more obvious, although the amplitude of WP5n is still rather weak. For the comparison

between EXP00 and EXP20, the cross section shows no obvious distinction during 110–114 h (cf. Figs. 13a,b and 13g,h). This period of no apparent wave difference along the short-dashed line is at least 8 h longer than that along the long-dashed line. At 118 h (Figs. 13c,i), the initial weak difference between EXP00 and EXP20 appears within 800–100 km near 10–12 km. At 122 h in EXP20 (Fig. 13j), a mature WP5nH-EXP20 (marked) can be identified near 12 km while WP5s in EXP20 above the tropopause seems to be amplified compared with that

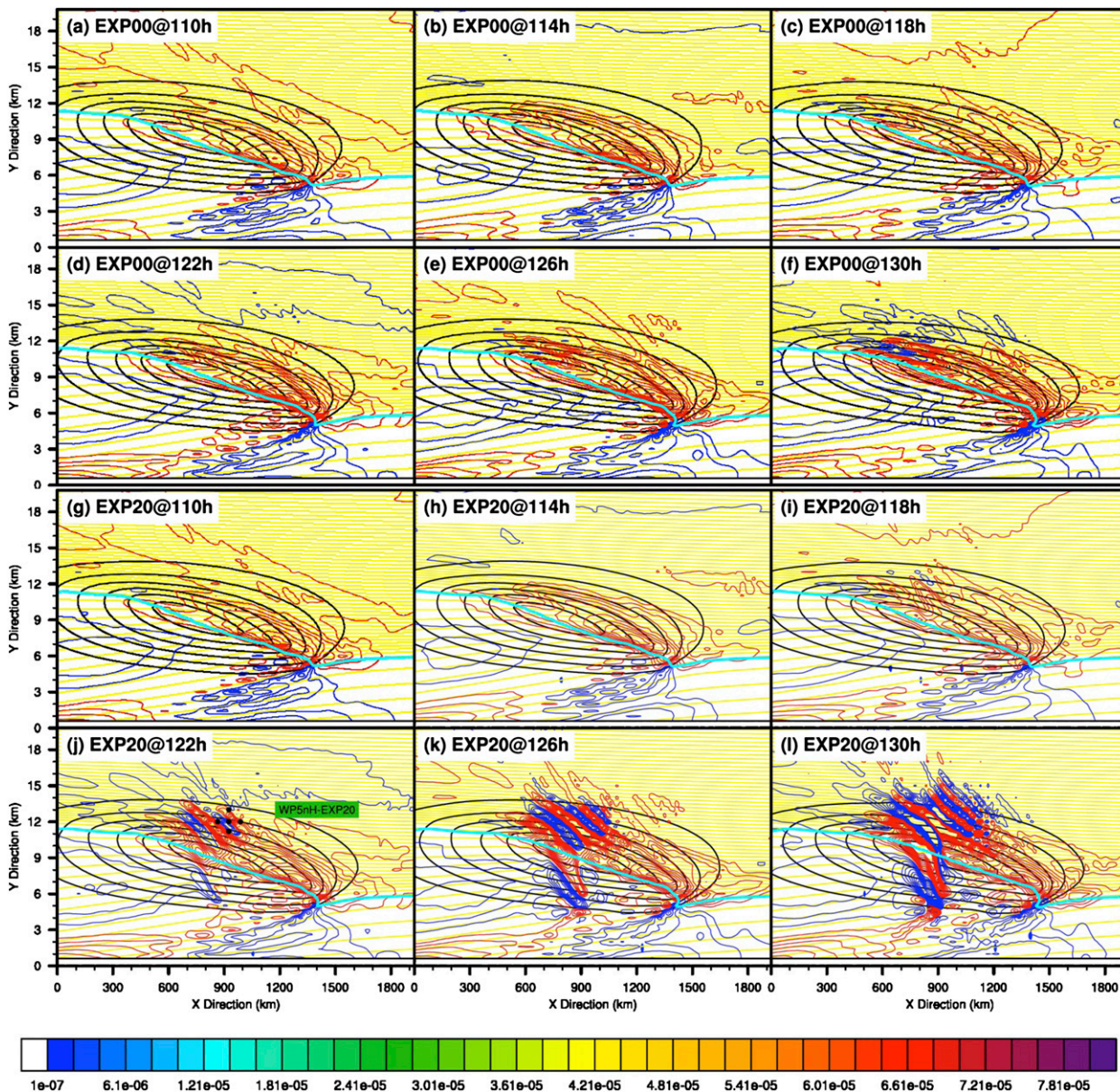


FIG. 13. As in Fig. 12, but for the green short-dashed line in Fig. 11. WP5nH-EXP20 is marked.

in EXP00 (Fig. 13d). During 122–130 h in EXP20 (Figs. 13j–l), the amplitudes of both WP5s and WP5n are gradually enhanced while they are traveling northward. It is interesting to see that there is a midtropospheric disturbance within 600–1200 km with no systematic latent heating release along the short-dashed line. On the contrary, the midtropospheric disturbance seems to accompany the local heating along the long-dashed line. Once again, this further suggests that localized latent heating release upstream may also impact the wave disturbance remotely where there is no latent heat release.

c. Evolution for WP3b-EXP20

The evolution of WP3b-EXP20 is traced back to 106 h to investigate its generation (Fig. 14). At 106 h (Fig. 14a), the effect of low-level latent heating release starts to initiate the response of a weak disturbance shown at 12 km. At 108 h (Fig. 14b), heating expands southward over the frontal system. With the 12-km divergence, weak waves can be identified above the colored heating edge. At 110 h (Fig. 14c), waves located at the edge of the growing heating are clearly enhanced. At 112 h (Fig. 14d), waves continue to propagate upward and

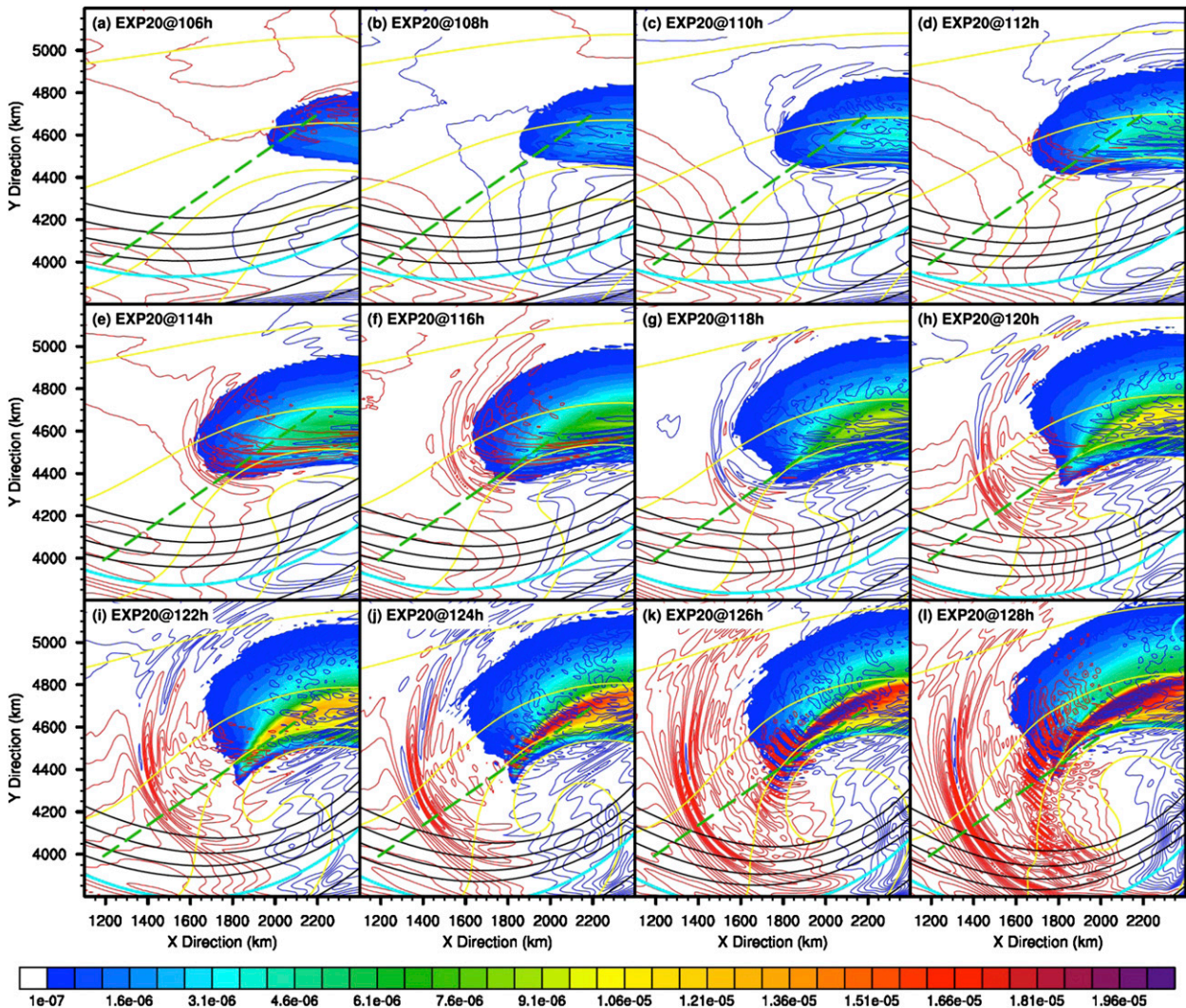


FIG. 14. Horizontal evolution of WP3b-EXP20 every 2 h from (a) 106 to (l) 128 h in EXP20. Contours follow Fig. 3, except that $\Delta = 5.0 \times 10^{-7} \text{ s}^{-1}$ for 12-km horizontal divergence. The shading denotes the vertically averaged positive-only latent heating rate (K s^{-1}).

travel toward the south. At 114 h (Fig. 14e), about one or two periods of wave-induced divergence perturbations appear to escape from the block of colored heating, and the vertical wavelengths of upward-propagating waves above the convection remarkably decrease within about 4 h (not shown). At 116 h (Fig. 14f), waves with relatively steep phase lines successfully escape from the convection, and the vertical wavelengths of nonescaping waves continue to decrease (not shown). Henceforth, escaping waves above the heating edge with weaker low-level disturbance should have longer vertical wavelengths than those of nonescaping waves directly above the heating with a stronger convective disturbance. At 118 h (Fig. 14g), at least two periods of wave-induced divergence perturbations are clearly observed away from the edge of convection, and they start to have bent phase

lines, similar to those in WP3b-EXP20 at 132 h. At 120 h (Fig. 14h), the area of colored heating almost stops expanding, and the heating maximum starts to have a tendency of being wrapped into the cyclone center. The aforementioned escaping waves travel southward and westward with the bended horizontal phase line nearly perpendicular to the 1-km temperature. At 122 h (Fig. 14i), the heating tends to be more centered over the northern part of the occluded front. The estimated speed of continually escaping wave packets along the green dashed line is approximately 50 km h^{-1} in the past 4 h. At 124 h (Fig. 14j), the radii of the bended phase lines in escaping waves gradually become larger as they propagate away from the heating. Above the strengthening localized convection at the edge of the color heating, there are new shorter-scale upward-propagating

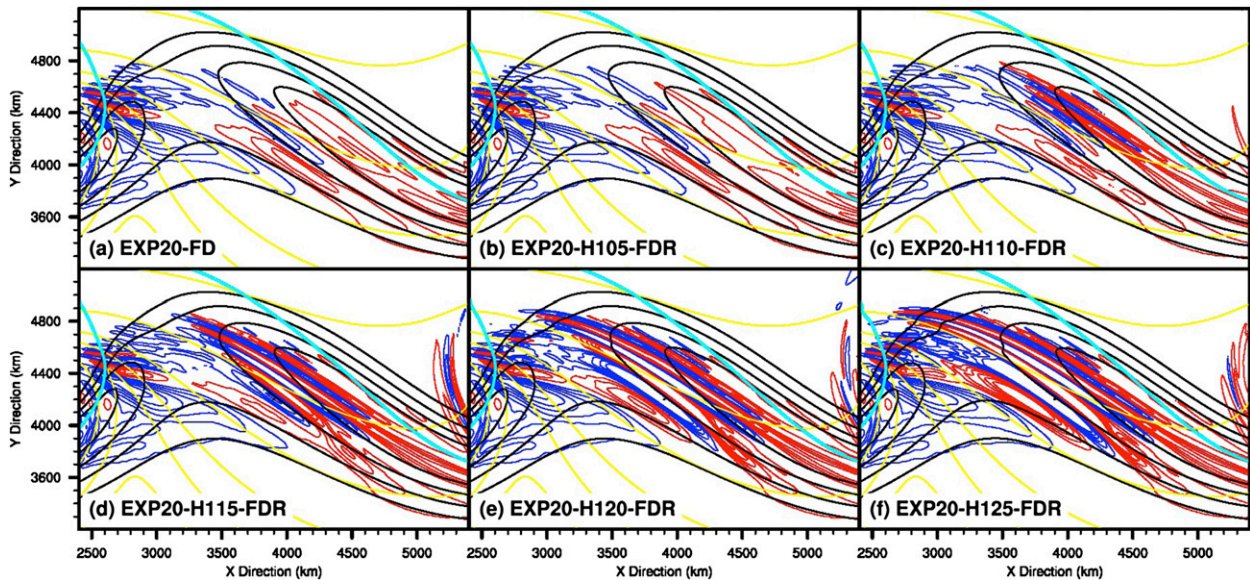


FIG. 15. Horizontal view of WP5 at 132 h in (a) EXP20-FD, (b) EXP20-H105-FDR, (c) EXP20-H110-FDR, (d) EXP20-H115-FDR, (e) EXP20-H120-FDR, and (f) EXP20-H125-FDR. Contours follow Fig. 3.

waves. During 126–128 h (Figs. 14k,l), new waves continue to escape from the heating, as developing convection modifies the surface front with the release of latent heating.

6. Sensitivity experiments

a. Sensitivity of WP5 to diabatic heating in EXP20

The sensitivity experiments applied to the moist process in this section include EXP20-DRY, EXP20-FD, EXP20-H105-FDR, EXP20-H110-FDR, EXP20-H115-FDR, EXP20-H120-FDR, EXP20-H125-FDR, and EXP20-H130-FDR. As illustrated by their names, EXP20-DRY (EXP20-FD) is a complete dry (fake dry) run from hour 0, and the other FDR experiments consist of full moist runs for 105–130 h and their restart runs without considering latent heating release. The main difference between EXP20 and EXP20-FD is determined by heating, while the difference between EXP20-FD and EXP20-DRY lies in the phase change and water-loading effect. The comparison between EXP20 and its corresponding sensitivity experiment is made at 132 h for WP5 and WP3b-EXP20, both of which are thought to be under the influence of moist processes judging from the distinction between EXP00 and EXP20. Since heating starts from about 103 h in EXP20, EXP20-H105-FDR possesses only 2 h of diabatic heating from convection and 27-h fake dry evolution affected by the accumulated effect of this 2-h heating. Similar interpretation can be applied into other fake dry restart runs.

In addition to EXP20 (Fig. 8c), Fig. 15 further demonstrates the horizontal comparison of WP5 among its various designed sensitivity tests at 132 h. No systematic distinction between EXP20-DRY (not shown) and EXP00 (Fig. 8a) is found at 132 h, so their initial-condition differences should contribute little to WP5's evolution in a dry atmosphere. Only minor differences can be observed between EXP20-DRY and EXP20-FD (Fig. 15a), especially for the location of the WP5s convergence peak. With the inclusion of only 2 h of diabatic heating from moist processes, EXP20-H105-FDR (Fig. 15b) has nearly the same WP5 structure and intensity as EXP20-FD. However, by including several more hours of diabatic heating in EXP20-H110-FDR (Fig. 15c), an apparent difference in WP5n is observed. With an additional 5 hours of diabatic heating from convection, the amplitude of WP5n in EXP20-H115-FDR (Fig. 15d) continues to be enhanced, and the structure of WP5s has also been adjusted. In EXP20-H120-FDR which has its diabatic heating cut off only after 120 h (Fig. 15e), the amplitude of WP5s is strengthened remarkably, and the western part of WP5n extends westward along the surface front. Finally, wave packets of WP5 in EXP20-H125-FDR (Fig. 15f) and EXP20-H130-FDR (not shown) with diabatic heating turned off at even later times are almost exactly the same as those in EXP20 at 132 h (Fig. 8c).

It is not surprising to find that the more latent heating that is allowed before starting the fake dry runs, the more similar WP5 in the fake dry runs is to that in EXP20. However, it is interesting that a distinct wave

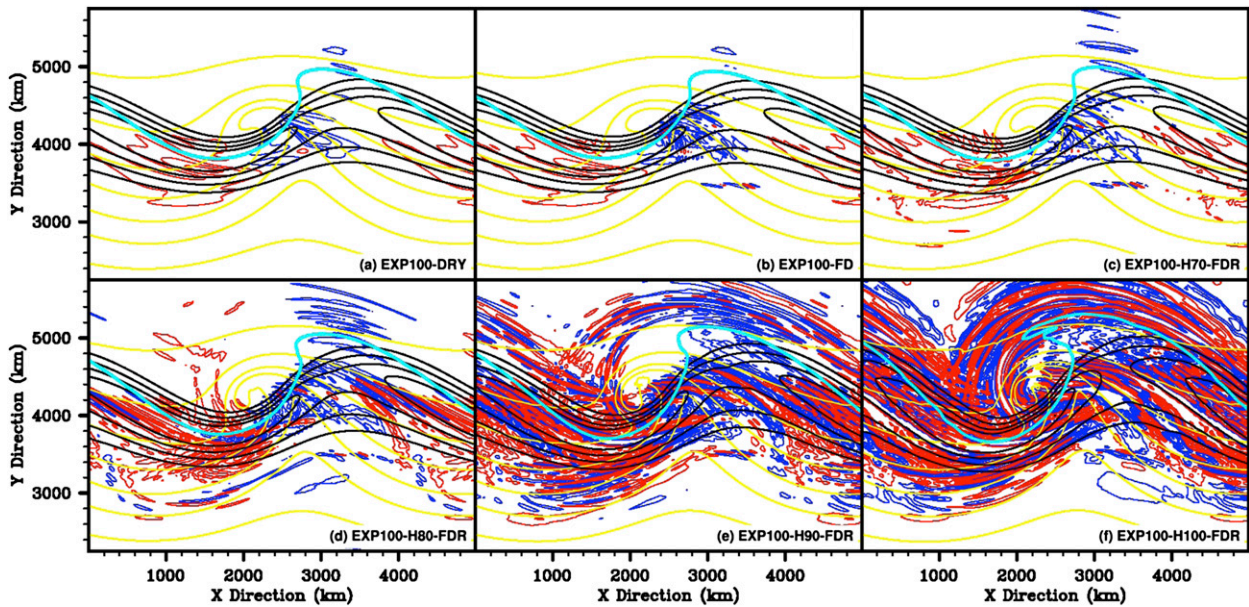


FIG. 16. Horizontal view comparison of (a) EXP100-DRY, (b) EXP100-FD, (c) EXP100-H70-FDR, (d) EXP100-H80-FDR, (e) EXP100-H90-FDR, and (f) EXP100-H100-FDR at 116 h. Contours follow Fig. 3.

response can be observed with only 7 h of heating accumulation after 22 h of fake dry physical processes. This result suggests that the impact of short-period convection may have a long-term impact on wave signals.

b. Sensitivity to the moist process in EXP100

In addition to EXP100 (Fig. 4d), Fig. 16 further demonstrates the horizontal divergence comparison among various designed sensitivity tests at 116 h. The sensitivity experiments to moist processes in this section include EXP100-DRY, EXP100-FD, EXP100-H70-FDR, EXP100-H80-FDR, EXP100-H90-FDR, and EXP100-H100-FDR. Although substantially similar to EXP100-DRY (Fig. 16a), EXP100-FD (Fig. 16b) is distinguished by random short-scale wave disturbances intertwined with the intermediate-scale jet-related gravity waves. This suggests that some fake dry processes, such as cloud formation, may also lead to additional wave disturbances, although they are much weaker without the release of latent heating. EXP100-H70-FDR (Fig. 16c) has nearly the same upper-level divergence signal as EXP100-FD, except for the minor differences above the frontal systems. With another 10 h of heating accumulation, the amplitude of WP5 in EXP100-H80-FDR (Fig. 16d) is larger, as is the amplitude of WP4. The delayed start of the fake dry simulation for another 10 h (EXP100-H90-FDR; Fig. 16e) will further enhance the amplitude of WP4, while short-scale waves to the north of the upper-level jet are intensified even more remarkably. For EXP100-H100-FDR (Fig. 16f), the above-mentioned

short-scale wave signals are noticeably strengthened over a much larger area. These findings of the sensitivity to moist process are generally consistent with past studies (e.g., Powers 1997) that found that diabatic heating is essential in amplifying the waves.

c. Sensitivity to enhanced horizontal resolution

We also performed several sensitivity experiments to investigate the enhanced horizontal resolution using 5-km grid spacing, including EXP00-5KM, EXP20-5KM, EXP40-5KM, EXP60-5KM, EXP80-5KM, and EXP100-5KM. Except for small differences in the gravity waves related to surface fronts, EXP00-5KM and EXP00 produce nearly identical mesoscale gravity waves (not shown). For those convection-related gravity waves discussed earlier (e.g., WP6-EXP20 and WP6-EXP100), their horizontal scales seem to remain unchanged (cf. Figs. 17a and 9a), while their amplitudes are enhanced to varying degrees, especially at the leading edge of the wave packet (cf. Figs. 17c and 9c). The amplification in short-scale wave amplitude can also be observed during the later stage of the baroclinic life cycle (not shown), likely due to stronger resolved convection with high resolution. Other new shorter-scale waves, likely tied to convective instability, have developed in the 5-km simulations (cf. Figs. 17b and 4b over the jet exit region along the warm front; cf. Figs. 17d and 4d in the jet exit region), which results in a wider wave-scale spectrum with enhanced horizontal resolution. Note that there is little sensitivity of medium-scale

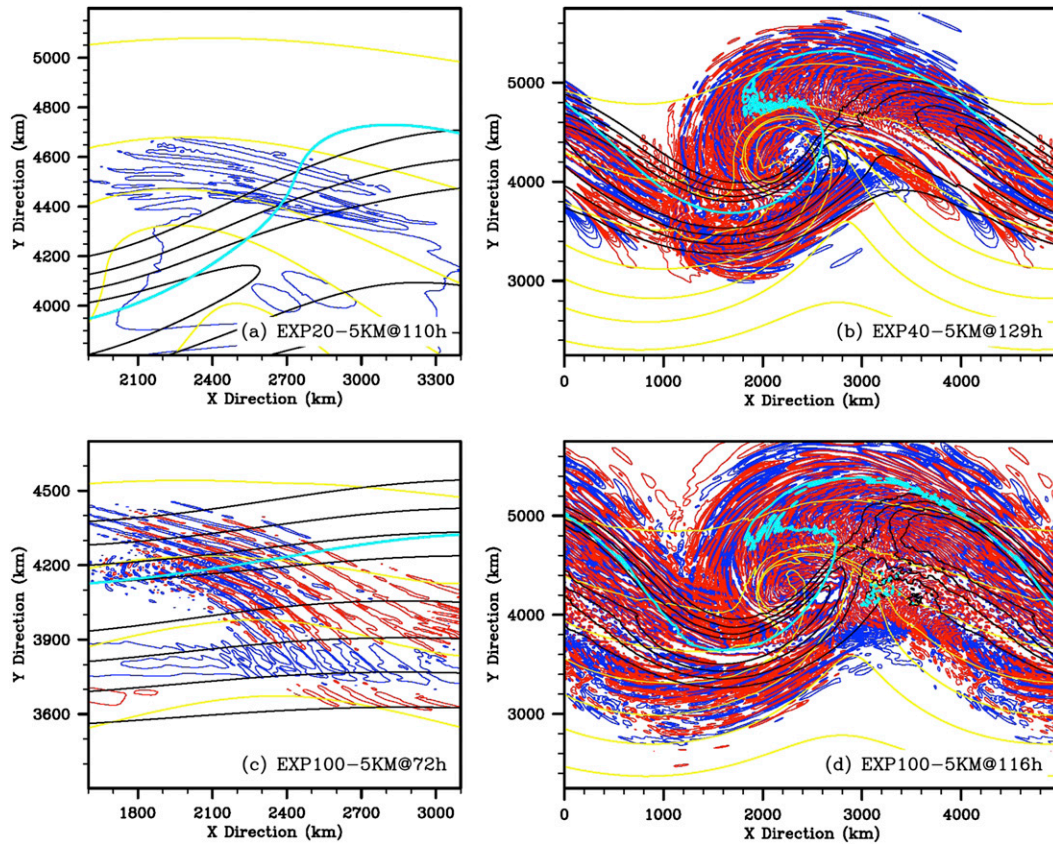


FIG. 17. Examples of horizontal snapshots in 5-km simulations (contours follow Fig. 3): (a) EXP20-5KM at 110 h, (b) EXP40-5KM at 129 h, (c) EXP100-5KM at 72 h, and (d) EXP100-5KM at 116 h.

waves to enhanced horizontal resolution, implying that they are being adequately resolved in 10-km simulations. Findings from these enhanced-resolution sensitivity experiments are largely consistent with the findings of past studies on this subject (e.g., Powers 1997; Zhang 2004; Plougonven and Snyder 2007).

7. Discussion on gravity wave variations under different convective instabilities

With particular emphasis on the difference between EXP00 and EXP20, this study presents a broad gravity wave comparison among six experiments with different initial moisture content. With the increase in baroclinic and convective instability as moisture content increases, gravity waves begin to couple and possibly interfere with each other as they propagate. For example, in EXP20 at 148 and 164 h (Figs. 3c,d), it is interesting to see that waves with different orientations appear to interfere with each other over a frontal boundary south of the jet-exit region. With less initial moisture content, the growth of EKE-GW is less efficient (Fig. 2b), partly due to a slower-growing EKE-BW (Fig. 2a). For example,

the EKE-GW in EXP20 and EXP00 take 146 (141, 140, 136) and 151 (145, 144, 139) h to reach similar amplitude to EXP100 (EXP80, EXP60, EXP40) at 116 (121, 126, 129) h. With the inclusion of moist convection as a new gravity wave source and a new contributor to the growing jet-front, the coupling of gravity waves becomes much stronger compared to drier environments.

Under no-moisture conditions in EXP00 and weak convective instability in EXP20, dry dynamic gravity wave modes dominate. The current research highlights the gravity wave comparison between EXP00 and EXP20 at the mature gravity wave stage. The locations and wave characteristics of WP1, WP2, and WP4 are almost identical between EXP00 and EXP20. Compared with the complete dry dynamics in EXP00, the convective mode (e.g., WP6-EXP20 at 110 h) in EXP20 is generated before the dry gravity wave modes become mature. For WP3 upstream of the convection, the locations and wave characteristics between WP3-EXP00 and WP3a-EXP20 are somewhat distinct from each other; another similar bended WP3b-EXP20 is also found to the west of the cyclone center. For WP5 downstream of the convection, wave amplitudes are noticeably

enhanced in EXP20, which implies that the convectively generated gravity waves can influence the downstream jet-related gravity waves. The enhancements or modifications in EXP20 of some particular wave modes are much more noticeable than the other wave modes. Two potential mechanisms are hypothesized in this discussion.

The first hypothesis is linked with the generation effect associated with enhanced localized baroclinic instability. Z04 proposed that the developing total baroclinic instability results in the increasing imbalance, which maximizes at the exit region of upper jet streak (near the strongest tropopause folding). Mesoscale gravity waves are continuously initiated downstream of the maximum imbalance. Spontaneous balance adjustment, as a generalization of the geostrophic adjustment (e.g., Rossby 1938; Cahn 1945; Blumen 1972; Kaplan and Paine 1977; Van Tuyl and Young 1982; Keyser and Shapiro 1986; UK87; Koch and Dorian 1988; OD95; Kaplan et al. 1997; Zhang et al. 2001), is hypothesized to be the likely mechanism in generating mesoscale gravity waves in the unbalanced tropospheric jet-front systems. In this hypothesis, the flow can become increasingly unbalanced after the gravity waves are being generated if the production of imbalance by the background flow outweighs the reduction of imbalance through the radiation of gravity waves. It is shown that the residual of the nonlinear balance equation (e.g., Zhang et al. 2000, 2001) can be used as an index of large-scale flow imbalance that spontaneously forces the gravity waves. However, even though one may argue that baroclinic instability in EXP20 is stronger than that in EXP00, especially after initial moist convection, it is particularly hard to explain why dry wave modes are only partially enhanced in EXP20. Therefore, modification needs to be performed. It is still possible that moist convection enhances localized baroclinic instability (e.g., localized jet or front) more efficiently. The enhanced gravity wave packets are excited by the localized imbalance with additional imbalance energy from convection.

The second hypothesis is linked with the propagation effect associated with the background flow. In EXP20, convection not only enhances the flow imbalance but also initiates a new gravity wave mode directly, noticeably at small scales but likely at intermediate scales as well. Convection-generated gravity waves in EXP20 propagate not only directly above the latent heating but also upstream and downstream of the latent heating. For example, WP6 is an example of convection-generated gravity waves directly above the latent heating. WP3b-EXP20 may be influenced by the upstream effect of convective gravity waves, and the enhancement in WP5 may be partially attributed to the downstream effect of convectively generated gravity waves. During wave

propagation, they are believed to interact with, strengthen, and modify the dry gravity wave mode, such as WP5 in EXP00 versus that in EXP20. The propagation effect of the background flow then further channels or transforms the full dry gravity wave modes in EXP00 to the modified dry gravity wave modes in EXP20. The propagation of convective gravity waves is largely determined by their wave characteristics, background flow, and the information of the source (e.g., location of the convection). For example, there is a remarkable resemblance between WP5s (Fig. 8; Table 1) and those experiments in Plougonven and Snyder (2007; their horizontal maps and cross sections in Fig. 3 and their wave characteristics calculation in Table 1). Plougonven and Snyder (2005) show that propagation effects of complex three-dimensional flow within similar regions can determine several characteristics of the gravity waves within similar regions. The effect is termed wave capture in Bühler and McIntyre (2005), following Badulin and Shrira (1993). Therefore, convective gravity waves may only be able to provide additional imbalance along their trajectory, which results in the partial enhancement or modification on the dry gravity wave modes. For example, WP2 is always located south of the convection, so little imbalance from convection travels through this area by background flow, which leads to the fact that the amplitude of WP2 is not remarkably strengthened.

Under enhanced but still moderate convective instability in EXP40 and EXP60, both shorter-scale waves and intermediate-scale waves are essential to the lower-stratosphere divergence. For example, in EXP40 at 129 h (Fig. 4b), the horizontal wavelength of divergence variances range from the short scale in the jet exit region to the intermediate scale south of the upper-level northwesterly jet. This feature is generally preserved by EXP60 at 126 h (Fig. 4c), but it interfered with more variance of shorter-scale gravity waves in the jet exit region. One can identify shorter-scale waves that are either parallel with or perpendicular to the tropopause/surface front. Not surprisingly, the shorter-scale waves in EXP60 cover a larger area than do those in EXP40.

Under strong convective instability in EXP80 and EXP100, the lower-stratosphere divergence manifests shorter-scale wave signatures filling the whole region of the baroclinic jet, instead of behaving as localized wave packets like those in EXP20. Convectively generated gravity waves (e.g., WP6-110EXP at 72 h) are observed much earlier than in EXP20. The convective mode is soon fully coupled with other gravity wave modes and background flow as baroclinicity increases over time. One example of the dominance of shorter-scale wave signatures is shown in EXP80 (e.g., Fig. 5d), although lower-stratosphere divergence in EXP80 still retains the

imprint of intermediate-scale wave signatures above the surface warm front south of the upper-level northwesterly jet. By contrast, in EXP100 at 116 h (Fig. 4d), it is particularly hard to determine the dominant orientation of the wave front above the surface warm front south of the upper-level northwesterly jet, probably due to the strengthening effect of the nonlinear wave–wave interaction. To the north of the above-mentioned region, the wave front orientations are almost parallel with the tropopause/surface front, with some exceptions that are perpendicular to the tropopause/surface front. To the south of the above-mentioned region, similar parallel tendencies between the wave front and surface front can also be found above the cold front. It is beyond the scope of the current study to distinguish and examine each of the complex wave modes in the experiments with high moisture content and strong convective instability.

There are several potential impacts of moisture on the generation and propagation of gravity waves. First, without latent heating, gravity waves differ only slightly among different experiments with different moisture content, most likely due to the initial relative humidity modification and the associated change in baroclinic growth rate. The fake dry process (e.g., the cloud formation) may also result in additional weak wave disturbances, as seen in the differences among experiments EXP00 (Fig. 8a), EXP20-DRY (not shown), EXP20-FD (Fig. 15a), EXP100-DRY (Fig. 16a), and EXP100-FD (Fig. 16b). Second, with the inclusion of latent heating, gravity waves generated in the dry atmosphere may be interacted with, strengthened, and modified by the newly generated convective gravity waves. Gravity waves, meanwhile, may also be modified or enhanced by stronger baroclinic instability and the local jet due to convection. One example of amplification in gravity wave amplitude due to moisture content is demonstrated in the comparison of WP5 between EXP00 and EXP20 (Fig. 8). The other potential consequence with the inclusion of moisture and diabatic heating, which is not examined in the current study but has been considered in previous studies (e.g., Durran and Klemp 1982; Jiang and Doyle 2009), is that dry gravity waves may be damped in the moisture layer due to destratification in the atmosphere and reduction in buoyancy frequency. In addition, one cannot rule out the possibility that dry gravity waves may also be partially canceled by the newly generated convective gravity waves during their propagation.

8. Concluding remarks

In this study, the ARW with high resolution (10-km horizontal grid spacing and about 300-m vertical grid spacing on average) is used to simulate the generation and propagation of mesoscale gravity waves from the

life cycles of moist baroclinic jet–front systems confined in a 4000-km periodic channel on an f plane. The model is initialized with a balanced 2D channeled baroclinic jet and its most unstable normal mode. Several experiments, using different initial moisture content, are compared in order to investigate the role of moist processes. The dry experiment with no moisture reproduces all five gravity wave modes simulated in the previous dry baroclinic jet–front systems. Under weak convective instability with a small amount of moisture, dry dynamic gravity wave modes continue to dominate. However, additional short-scale wave packets, probably generated by moist convection, are observed about 30 h before dry gravity wave modes become mature. For gravity waves downstream of the convection, wave amplitudes are noticeably enhanced, likely due to the interaction between convection and dry dynamics. The partial enhancements or modifications of some particular wave modes may either be due to the enhanced wave generation associated with enhanced localized baroclinic instability or in response to the propagation effect associated with a modified background flow. The fake dry experiment further demonstrates that the period and amount of latent heating from moist processes largely determines its simulated wave amplitude. Under strong convective instability with full moisture content, convection-generated gravity waves are observed much earlier than are those with reduced moisture content. The convective mode is soon fully coupled with other gravity wave modes and background flow as baroclinicity increases over time. Therefore, the upper-troposphere and lower-stratosphere divergence manifests shorter-scale wave signatures, which fill the whole region of the baroclinic jet.

Future research will continue to evaluate the generation effect with linear models (e.g., Wang et al. 2010), to examine the propagation effect with a gravity wave–tracing model (e.g., Marks and Eckermann 1995; LZ08), to better analyze the properties of the gravity waves through spectral or wavelet analysis (e.g., Zhang et al. 2001), and to better understand and parameterize the impacts of the gravity waves in the moist baroclinic jet–front systems.

Acknowledgments. We are very grateful to Shuguang Wang for help setting up the experiments and to Y. Qiang Sun and three anonymous reviewers for their insightful comments. This research is supported by the National Science Foundation under Grants 0904635 and 1114849.

REFERENCES

- Badger, J., and B. J. Hoskins, 2001: Simple initial value problems and mechanisms for baroclinic growth. *J. Atmos. Sci.*, **58**, 38–49.

- Badulin, S. I., and V. I. Shrira, 1993: On the irreversibility of internal waves dynamics due to wave-trapping by mean flow inhomogeneities. Part I. Local analysis. *J. Fluid Mech.*, **251**, 21–53.
- Blumen, W., 1972: Geostrophic adjustment. *Rev. Geophys. Space Phys.*, **10**, 485–528.
- Bosart, L. F., W. E. Bracken, and A. Seimon, 1998: A study of cyclone mesoscale structure with emphasis on a large-amplitude inertia-gravity waves. *Mon. Wea. Rev.*, **126**, 1497–1527.
- Bühler, O., and M. E. McIntyre, 2005: Wave capture and wave-vortex duality. *J. Fluid Mech.*, **534**, 67–95.
- Cahn, A., 1945: An investigation of the free oscillations of a simple current system. *J. Meteor.*, **2**, 113–119.
- Davis, C. A., and K. A. Emanuel, 1991: Potential vorticity diagnosis of cyclogenesis. *Mon. Wea. Rev.*, **119**, 1929–1952.
- Dudhia, J., 1993: A nonhydrostatic version of the Penn State-NCAR Mesoscale Model: Validation tests and simulation of an Atlantic cyclone and cold front. *Mon. Wea. Rev.*, **121**, 1493–1513.
- Durran, D. R., and J. B. Klemp, 1982: On the effects of moisture on the Brunt-Väisälä frequency. *J. Atmos. Sci.*, **39**, 2152–2158.
- Eliassen, A., and E. Palm, 1961: On the transfer of energy in stationary mountain waves. *Geophys. Publ.*, **22**, 1–23.
- Fritts, D. C., and G. D. Nastrom, 1992: Sources of mesoscale variability of gravity waves. Part II: Frontal, convective, and jet stream excitation. *J. Atmos. Sci.*, **49**, 111–127.
- , and M. J. Alexander, 2003: Gravity wave dynamics and effects in the middle atmosphere. *Rev. Geophys.*, **41**, 1003, doi:10.1029/2001RG000106.
- Gill, A. E., 1982: *Atmosphere-Ocean Dynamics*. Academic Press, 488 pp.
- Holton, J. R., P. H. Haynes, M. E. McIntyre, A. R. Douglass, R. B. Road, and L. Pfister, 1995: Stratosphere-troposphere exchange. *Rev. Geophys.*, **33**, 403–439.
- Hooke, W. H., 1986: Gravity waves. *Mesoscale Meteorology and Forecasting*, P. S. Ray, Ed., Amer. Meteor. Soc., 272–288 pp.
- Jewett, B. F., M. K. Ramamurthy, and R. M. Rauber, 2003: Origin, evolution, and finescale structure of the St. Valentine's Day mesoscale gravity wave observed during STORM-FEST. Part III: Gravity wave genesis and the role of evaporation. *Mon. Wea. Rev.*, **131**, 617–633.
- Jiang, Q., and J. D. Doyle, 2009: The impact of moisture on mountain waves during T-REX. *Mon. Wea. Rev.*, **137**, 3888–3906.
- Kaplan, M. L., and D. A. Paine, 1977: The observed divergence of the horizontal velocity field and pressure gradient force at the mesoscale. *Beitr. Phys. Atmos.*, **50**, 321–330.
- , S. E. Koch, Y.-L. Lin, R. P. Weglarz, and R. A. Rozumalski, 1997: Numerical simulations of a gravity wave event over CCOPE. Part I: The role of geostrophic adjustment in mesoscale jetlet formation. *Mon. Wea. Rev.*, **125**, 1185–1211.
- Keyser, D., and M. A. Shapiro, 1986: A review of the structure and dynamics of upper-level frontal zones. *Mon. Wea. Rev.*, **114**, 452–499.
- Kim, Y.-J., S. D. Eckermann, and H.-Y. Chun, 2003: An overview of the past, present and future of gravity-wave drag parameterization for numerical climate and weather prediction models. *Atmos.-Ocean*, **41**, 65–98.
- Klemp, J. B., J. Dudhia, and A. D. Hassiotis, 2008: An upper gravity-wave absorbing layer for NWP applications. *Mon. Wea. Rev.*, **136**, 3987–4004.
- Koch, S. E., and P. B. Doran, 1988: A mesoscale gravity wave event observed during CCOPE. Part III: Wave environment and probable source mechanisms. *Mon. Wea. Rev.*, **116**, 2570–2592.
- , F. Zhang, M. Kaplan, Y.-L. Lin, R. Weglarz, and M. Trexler, 2001: Numerical simulation of a gravity wave event observed during CCOPE. Part III: The role of a mountain-plains solenoid in the generation of the second wave episode. *Mon. Wea. Rev.*, **129**, 909–932.
- , and Coauthors, 2005: Turbulence and gravity waves within an upper-level front. *J. Atmos. Sci.*, **62**, 3885–3908.
- Koppel, L. L., L. F. Bosart, and D. Keyser, 2000: A 25-yr climatology of large-amplitude hourly surface pressure changes over the conterminous United States. *Mon. Wea. Rev.*, **128**, 51–68.
- Lane, T. P., and M. J. Reeder, 2001: Convectively generated gravity waves and their effect on the cloud environment. *J. Atmos. Sci.*, **58**, 2427–2440.
- , and F. Zhang, 2011: Coupling between gravity waves and tropical convection at mesoscales. *J. Atmos. Sci.*, **68**, 2582–2598.
- , J. D. Doyle, R. Plougonven, M. A. Shapiro, and R. D. Sharman, 2004: Observations and numerical simulations of inertia-gravity waves and shearing instabilities in the vicinity of a jet stream. *J. Atmos. Sci.*, **61**, 2692–2706.
- Lin, Y., and F. Zhang, 2008: Tracking gravity waves in baroclinic jet-front systems. *J. Atmos. Sci.*, **65**, 2402–2415.
- Lin, Y.-L., R. D. Farley, and H. D. Orville, 1983: Bulk parameterization of the snow field in a cloud model. *J. Climate Appl. Meteor.*, **22**, 1065–1092.
- Marks, C. J., and S. D. Eckermann, 1995: A three-dimensional nonhydrostatic ray-tracing model for gravity waves: Formulation and preliminary results for the middle atmosphere. *J. Atmos. Sci.*, **52**, 1959–1984.
- O'Sullivan, D., and T. J. Dunkerton, 1995: Generation of inertia-gravity waves in a simulated life cycle of baroclinic instability. *J. Atmos. Sci.*, **52**, 3695–3716.
- Plougonven, R., and C. Snyder, 2005: Gravity waves excited by jets: Propagation versus generation. *Geophys. Res. Lett.*, **32**, L18802, doi:10.1029/2005GL023730.
- , and —, 2007: Inertia-gravity waves spontaneously generated by jets and fronts. Part I: Different baroclinic life cycles. *J. Atmos. Sci.*, **64**, 2502–2520.
- , and F. Zhang, 2014: Internal gravity waves from jets and fronts. *Rev. Geophys.*, doi:10.1002/2012RG000419, in press.
- , H. Teitelbaum, and V. Zeitlin, 2003: Inertia gravity wave generation by tropospheric midlatitude jet as given by the Fronts and Atlantic Storm-Track Experiment radio soundings. *J. Geophys. Res.*, **108**, 888–889.
- Pokrandt, P. J., G. J. Tripoli, and D. D. Houghton, 1996: Processes leading to the formation of mesoscale waves in the Midwest cyclone of 15 December 1987. *Mon. Wea. Rev.*, **124**, 2726–2752.
- Powers, J. G., 1997: Numerical model simulation of a mesoscale gravity wave event: Sensitivity tests and spectral analysis. *Mon. Wea. Rev.*, **125**, 1838–1869.
- , and R. J. Reed, 1993: Numerical model simulation of the large-amplitude mesoscale gravity-wave event of 15 December 1987 in the central United States. *Mon. Wea. Rev.*, **121**, 2285–2308.
- Ramamurthy, M. K., R. M. Rauber, B. Collins, and N. K. Malhotra, 1993: A comparative study of large-amplitude gravity-wave events. *Mon. Wea. Rev.*, **121**, 2951–2974.
- Rauber, R. M., M. Yang, M. K. Ramamurthy, and B. F. Jewett, 2001: Origin, evolution, and fine-scale structure of the St. Valentine's Day mesoscale gravity wave observed during STORM-FEST. Part I: Origin and evolution. *Mon. Wea. Rev.*, **129**, 198–217.

- Rosby, C. G., 1938: On the mutual adjustment of pressure and velocity distributions in certain simple current systems, ii. *J. Mar. Res.*, **5**, 239–263.
- Schneider, R. S., 1990: Large-amplitude mesoscale wave disturbances within the intense Midwest extratropical cyclone of 15 December 1987. *Wea. Forecasting*, **5**, 533–558.
- Shapiro, M. A., 1980: Turbulent mixing within tropopause folds as a mechanism for the exchange of chemical constituents between the stratosphere and troposphere. *J. Atmos. Sci.*, **37**, 994–1004.
- , and D. Keyser, 1990: Fronts, jet streams, and the tropopause. *Extratropical Cyclones: The Erik Palmén Memorial Volume*, C. W. Newton and E. O. Holopainen, Eds., Amer. Meteor. Soc., 167–191.
- Simmons, A. J., and B. J. Hoskins, 1978: The life cycles of some nonlinear baroclinic waves. *J. Atmos. Sci.*, **35**, 414–432.
- Skamarock, W. C., and Coauthors, 2008: A description of the Advanced Research WRF version 3. NCAR Tech. Note NCAR/TN-475+STR, 113 pp.
- Tan, Z., F. Zhang, R. Rotunno, and C. Snyder, 2004: Mesoscale predictability of moist baroclinic waves: Experiments with parameterized convection. *J. Atmos. Sci.*, **61**, 1794–1804; Corrigendum, **65**, 1479.
- Uccellini, L. W., and S. E. Koch, 1987: The synoptic setting and possible source mechanisms for mesoscale gravity wave events. *Mon. Wea. Rev.*, **115**, 721–729.
- Van Tuyl, A. H., and J. A. Young, 1982: Numerical simulation of nonlinear jet streak adjustment. *Mon. Wea. Rev.*, **110**, 2038–2054.
- Waite, M. L., and C. Snyder, 2013: Mesoscale energy spectra of moist baroclinic waves. *J. Atmos. Sci.*, **70**, 1242–1256.
- Wang, S., and F. Zhang, 2007: Sensitivity of mesoscale gravity waves to the baroclinicity of jet-front systems. *Mon. Wea. Rev.*, **135**, 670–688.
- , —, and C. C. Epifanio, 2010: Forced gravity wave response near the jet exit region in a linear model. *Quart. J. Roy. Meteor. Soc.*, **136**, 1773–1787.
- Wu, D. L., and F. Zhang, 2004: A study of mesoscale gravity waves over the North Atlantic with satellite observations and a mesoscale model. *J. Geophys. Res.*, **109**, D22104, doi:10.1029/2004JD005090.
- Zhang, D. L., and J. M. Fritsch, 1988: Numerical simulation of the meso- β scale structure and evolution of the 1977 Johnstown flood. Part III: Inertial gravity waves and the squall line. *J. Atmos. Sci.*, **45**, 1252–1268.
- Zhang, F., 2004: Generation of mesoscale gravity waves in the upper-tropospheric jet-front systems. *J. Atmos. Sci.*, **61**, 440–457.
- , and S. E. Koch, 2000: Numerical simulation of a gravity wave event over CCOPE. Part II: Wave generated by an orographic density current. *Mon. Wea. Rev.*, **128**, 2777–2796.
- , —, C. A. Davis, and M. L. Kaplan, 2000: A survey of unbalanced flow diagnostics and their application. *Adv. Atmos. Sci.*, **17**, 165–183.
- , —, —, and —, 2001: Wavelet analysis and the governing dynamics of a large-amplitude gravity wave event along the east coast of the United States. *Quart. J. Roy. Meteor. Soc.*, **127**, 2209–2245.
- , —, and M. L. Kaplan, 2003: Numerical simulations of a large-amplitude gravity wave event. *Meteor. Atmos. Phys.*, **84**, 199–216.
- , N. Bei, R. Rotunno, C. Snyder, and C. C. Epifanio, 2007: Mesoscale predictability of moist baroclinic waves: Convection-permitting experiments and multistage error growth dynamics. *J. Atmos. Sci.*, **64**, 3579–3594.
- , M. Zhang, J. Wei, and S. Wang, 2013: Month-long simulations of gravity waves over North America and North Atlantic in comparison with satellite observations. *Acta Meteor. Sin.*, **27**, 446–454.